

Understanding The Surface Integrity of Laser Surface Engineered Tungsten Carbide

Kafayat E Hazzan

Loughborough University

Manuela Pacella (✉ M.Pacella@lboro.ac.uk)

Loughborough University <https://orcid.org/0000-0002-5775-1038>

Tian L See

The Manufacturing Technology Centre (MTC) Ltd.

Research Article

Keywords: Tungsten carbide, Laser processing, Surface optimisation, Laser modelling, Surface integrity, Crack formation

Posted Date: May 18th, 2021

DOI: <https://doi.org/10.21203/rs.3.rs-425549/v1>

License:  This work is licensed under a Creative Commons Attribution 4.0 International License.

[Read Full License](#)

Version of Record: A version of this preprint was published at The International Journal of Advanced Manufacturing Technology on September 14th, 2021. See the published version at <https://doi.org/10.1007/s00170-021-07885-8>.

Abstract

The study investigated the effect of fibre laser processing (1060 nm, 240 ns pulse duration) on tungsten carbide (WC). Fluence, frequency, and the interaction effect of these were the most influential factors on the surface integrity and crack formation. In this paper, a crack classification system was developed, and a crack density variable was introduced to estimate the number of cracks and crack type within a 1 mm² area size. ANOVA was used to analyse how fluence (0.05–0.20 J/cm²) and frequency (5–100 kHz) altered the crack density. The crack density increased between 0.050–0.099 J/cm² across all frequency settings then decreased as the fluence increased to 0.20 J/cm². Superficial cracks were present in all frequency settings but particularly with lower fluence settings. Micro-cracks were more likely to form between 0.050–0.135 J/cm². Deep cracks did not present until 40 kHz or above 0.099 J/cm² across the frequency settings and were situated around balling and splatter defects. The crack density was minimised at 0.149 J/cm² fluence and 52.5 kHz. To the author's knowledge for the first time a quantitative analysis of the crack formation mechanism for brittle materials is proposed (post laser processing). In addition, a linear model generated to predict surface roughness performed best at moderate to medium level of processing (fluences in the region of 0.050–0.099 J/cm²) with an error between 1 % to 10 %. The model failed to predict the material response as accurately at higher fluences with percentage errors between 15 % to 36 %.

Introduction

Tungsten Carbide (WC) is classified as a hard ceramic metal, the binders used in sintering add toughness properties to offset the brittle nature of the ceramic. It is the most widely utilised cutting tool material in a range of applications: turning, milling, high speed cutting and high value manufacturing [1]. The unique characteristic of having both metallic and ceramic properties give WC high strength, durability and the ability to withstand high temperatures [2]. Lasers cutting by ablation is a precise and non-contact method able to make clean and complex cuts [3]; despite this, the process can induce both mechanical and thermal defects. In WC these microstructural defects are mainly thermal shock [4], cracking, porosity [5], recast layer and heat affected zone (HAZ) [1] also due to the polycrystalline structure.

Tools need to be manufactured to small tolerances to produce the desired geometry on a workpiece surface. Often this is difficult to do without inducing microstructural defects which limit the tool performance and life [2]. These defects act as stress raisers and points of crack initiations, as cutting tools are subjected to large loads and forces. Sigl and Exner [6] analysed the fracture path of WC with different weight percentages of cobalt 6–15 %. It showed that the fracture behaviour was dominated by the brittle nature of the WC phase, initiating in the intergranular and transgranular regions, causing voids in the softer cobalt phases. Herd et al. [7] drew the same conclusions when simulating WC-Co fracture. Stress concentrations made cracks grow along the WC-Co boundaries and propagated along the WC/WC and WC/Co boundaries.

These studies highlight defects purely from mechanical loading but the heat from laser processing is an additional factor to consider given the additional energy transfer during the process. During laser processing materials undergo thermal expansion, it expands during heating phases and contracts during cooling/resolidification stages [8]. If this is in an uncontrolled manner, a phenomenon known as thermal shock occurs; this is particularly of concern with composite materials like WC [9]. If there is a significant difference in the expansion rates, one material will expand while the other expands to a smaller extent. The second material cannot expand further, it must fracture leading to crack formation within the microstructure. Lee et al. [10] demonstrated the effects of a thermal mismatch when laser cladding WC-NiCr on STS410 steel. The study found that the differences in thermal expansion between the matrix and the binder caused high stress during the solidification of the clad track. This made the clad inherently weaker allowing for small cracks to propagate through the structure. Hasselman [11] conducted a thorough investigation into thermal shock in brittle ceramics and the formation of fractures and cracks. The study found that thermal stress fracture is relatively easy to induce in these materials and the thermal shock behaviour is quite unpredictable. The study also developed a critical temperature difference (ΔT) formula to relate crack instability with temperature. Stating that there is minimum thermal strain required to induce short cracks (ΔT_{c1}) and induce long cracks (ΔT_{c2}). If the temperature change is below ΔT_{c1} , there should be no change in crack length from an initial point, remaining stable. Between ΔT_{c1} and ΔT_{c2} cracks grow in a quasi-static manner. Past ΔT_{c2} the crack growth will be catastrophic. Wang et al. [12] investigated the high temperature fracture mechanism of WC-Co. The samples were placed in a 3-point bending jig at temperatures ranging from 300°C to 900°C. The temperature affected the speed of crack growth. At higher temperatures material degradation by oxidation occurred, more damage at crack points and cobalt softening were present. The temperature reached during laser processing is determined by the energy parameters selected to enable ablation. Dumitru et al. [13] determined the ablation threshold of various ultrahard materials using a femtosecond laser. WC-Co10 % and WC-Co6 % had a threshold of 0.4 J/cm² and 0.3 J/cm² respectively. The study found that increasing the fluence from 0.4–2.8 J/cm² caused a higher surface roughness with large pores in the processing crater and physical damage on the surface. Lickschat et al. [14] investigated the use of a picosecond laser on stainless steel and tungsten carbide with fluences up to 10 J/cm². It found that by changing the laser parameters: pulse number, wavelength and pulse duration, the material removal efficiency was improved. For example, changing the pulse duration from 10 ps to 0.2 ps increased the ablation depth from 13 nm to 32 nm, respectively. Marimuthu et al. [1] used a picosecond laser to machine WC. Increasing the laser fluence between 1.27–17.3 J/cm² increased the ablation depth and surface roughness of the achieved grooves. Also, a simultaneous increase of frequency and speed created a better quality with no significant thermal defects e.g., recast layer, microcracks and HAZ. The study also found that the material removal rate was proportional to the average laser power. Thus, the quality of process and resulting surface integrity was improved via optimisation of laser parameters. The effect of laser parameters has also been seen in other laser applications, for example selective laser sintering (SLS). Ditsche and Seefeld [15] used a pulsed laser to cause recrystallisation to form agglomerates in WC powder. The power was varied between 2.75–3.25 kW. The lower power made small

agglomerates form with an inhomogeneous heat conduction. The higher power increased the size of the masses allowing for a better WC structure; but the excess heat also promoted formation of other WC phases of W₂C.

Current methods in choosing the right process parameters rely on human judgement or selectively testing possible settings and determining the right combination which gives the desired result. Previous studies have used various analytical techniques including design of experiments (DOE) methods and ANOVA to examine the effect of laser parameters in the laser ablation of hard and ultra-hard materials for example Wang et al. [16] on PCBN, Pacella et al. [17] on PCD, Karpuschewski et al. [18] and Kacar et al. [19] on ceramic tools. Simple DOE setups (e.g., 2³ or 2⁴ factorials) can indicate the amount of variation a factor has on a dependent variable. ANOVA is a widely used statistical tool to understand how significant each factor is to a response variable relying on the variance within datasets and variables. DOE and ANOVA are simpler and easier statistical tools to understand multi-variate behaviour compared to Finite element approaches which require high computational input and expertise. Wang et al. [16] used a 2³ fractional DOE experiment to optimise a hybrid laser waterjet process on PCBN materials. Laser power and waterjet pressure were the most significant factors on the cut quality. Altering these parameters improved the cut quality reducing taper and HAZ thereby enhancing the control on phase transformation and propagation. Calderón Urbina et al. [20] conducted an analytical investigation into the material removal rate of laser ablation on WC. Laser power, burst-mode pulse overlaps and scanning pattern were the factors of interest. It concluded that the laser power and overlap were the most influential variables in the cutting process.

Previous research shows that even simple modelling provides an objective and reproducible methodology to understanding a process and material behaviour. However, fewer works have reported the optimisation of laser parameters for brittle materials (i.e., WC) based on crack formation and surface integrity. In cutting tools cracking is a type of surface defect that strongly hinders tool performance, therefore optimising and controlling the laser process to avoid crack formation is needed as studies have done in other materials [21].

1.1. Scope of the paper

Laser manufacturing of WC requires a thorough understanding of WC behaviour to improve the quality of the process and ensure that resultant microstructure does not have an adverse effect on the cutting tool performance. WC is inherently brittle and falls under the group of materials that will fracture under thermal effects. The cemented carbides response to mechanical and electrical processes e.g., grinding, turning, electrical discharge machining (EDM), and electrochemical machining (ECM) has been greatly reviewed but limited research is reported on WC response to laser-beam processes i.e. heating and melting. The objectives of the research paper are:

- To experimentally investigate the effect of laser parameters on the surface morphology and integrity on a WC cutting tool material using a pulse fibre laser (1060 nm wavelength, 70 W maximum output

power). The parameters chosen were fluence, frequency, feed speed and hatch distance. This includes the analysis of surface crack generation based on the most influential factors to the surface roughness.

- Generate a numerical linear model to predict the surface roughness in relation to the distribution of surface peaks generated by laser processing, using DOE optimisation techniques.
- To investigate the crack formation and fracture behaviour of WC using ANOVA by developing a new method for classifying surface cracks produced from laser processing.

Methodology

2.1. Material

The study used a WC-Co12 % blank (Ultra-met Z57 corresponding to an industrial grade C5 based on ANSI standard) with a mean grain size of 4 μm . This grade is typically used in turning and milling on softer alloyed materials at medium speeds [2]. The chemical composition of the sample, measured by Energy Dispersive Spectroscopy (EDS), is given in Table 1.

Table 1
Chemical composition of unprocessed WC-Co12 % disk.

Element	W	C	Co	O	Al	Fe	Si
wt%	41.6	24.0	12.4	15.8	2.2	2.2	1.8

2.2. Laser Machining

A 70 W InnoLas MMS single mode SPI fibre laser 1060 nm was used, with a beam mode profile of $M^2 < 1.6$. The laser is equipped with pre-programmed waveforms. Waveform 0 was used as a default setting: pulse duration of 240 ns, max pulse energy 1 mJ; this gives a maximum fluence of 0.20 J/cm². This is lower than the WC ablation threshold of 0.45 J/cm² in the ns regime [13], thus laser mechanism discussed in this paper focused on melting and partial ablation of the binder. The beam diameter at the focal height of 60.5 mm was 80 μm , the generated laser fluences were calculated based on previous research from Pacella et al. [22]. A 1 mm² square was processed for each experiment using 1 pass in a path pattern shown in Fig. 1a.

2.2.1. Experiment design

A 2^4 factorial design consisted of 4 factors (fluence, frequency, speed, and hatch distance) with 2 levels, giving 16 experimental conditions, repeated 3 times. All other laser parameters and conditions were kept constant, including the number of scan repetitions and laser spot size. Table 2 and Table 3 outlines the parameter settings for each experiment. A reference experiment was also conducted between the 2 levels of each factor. The low and high level of hatch distances and feed speed give an overlap of 83.40 % and 49.97 % respectively, calculated based on previous research Dahotore and Marimkar [23].

Table 2
DOE experiment levels.

Factors of interest	Units	Symbol	Low level (-1)	High level (1)
Fluence	J/cm ²	Ψ	0.050	0.149
Repetition frequency	kHz	f	17.5	52.5
Feed speed	mm/s	v	500	1500
Hatch Distance	mm	d	0.02	0.06

Table 3
Parameter settings for each experiment with 2⁴ design.

Experiment	Ψ	Fluence	f	Frequency	v	Speed	d	Hatch
0	0	0.099	0	35.0	0	1000	0	0.04
1	-1	0.050	-1	17.5	-1	500	-1	0.02
2	1	0.149	-1	17.5	-1	500	-1	0.02
3	-1	0.050	1	52.5	-1	500	-1	0.02
4	-1	0.050	-1	17.5	1	1500	-1	0.02
5	-1	0.050	-1	17.5	-1	500	1	0.06
6	1	0.149	1	52.5	-1	500	-1	0.02
7	1	0.149	-1	17.5	1	1500	-1	0.02
8	1	0.149	-1	17.5	-1	500	1	0.06
9	-1	0.050	1	52.5	1	1500	-1	0.02
10	-1	0.050	1	52.5	-1	500	1	0.06
11	-1	0.050	-1	17.5	1	1500	1	0.06
12	1	0.149	1	52.5	1	1500	-1	0.02
13	-1	0.050	1	52.5	1	1500	1	0.06
14	1	0.149	-1	17.5	1	1500	1	0.06
15	1	0.149	1	52.5	-1	500	1	0.06
16	1	0.149	1	52.5	1	1500	1	0.06

The DOE experiment also acted as a screening test to identify the main parameters affecting the microstructure and surface integrity, leading to further experimental designs. The second set of

experiment (Table 4) focuses on understanding the material response to irradiance with fluence and frequency ($v = 500 \text{ mm/s}$, $d = 0.02 \text{ mm}$). An orthogonal array of 49 experiments was made with 7 settings for both factors; to highlight the micro-crack generation, crack density and microstructural characteristics. It was repeated 3 times to increase robustness. Analysis of Variance (ANOVA) was also utilised to identify the amount of variation on crack density based on changing the parameter values, and the significance of each factor.

Table 4 – Experiment number for comparing fluence and frequency for understanding material crack generation ($v = 500 \text{ mm/s}$, $d = 0.02 \text{ mm}$).

Experiment number							
Fluence (J/cm^2)	0.030	0.050	0.070	0.099	0.135	0.149	0.200
Frequency (kHz)							
5.0	1	8	15	22	29	36	43
17.5	2	9	16	23	30	37	44
28.0	3	10	17	24	31	38	45
40.0	4	11	18	25	32	39	46
52.5	5	12	19	26	33	40	47
75.0	6	13	20	27	34	41	48
100.0	7	14	21	28	35	42	49

The feed speed was also investigated independently to understand other material phenomenon, with 6 experiments varied between 250 mm/s and 2500 mm/s ($\psi = 0.050 \text{ J/cm}^2$, $f = 52.5 \text{ kHz}$, $d = 0.02 \text{ mm}$), repeated 3 times (Taguchi orthogonal array).

2.3. Characterisation

The samples were cleaned with an acetone solution to remove dirt and debris prior to characterisation. The surface roughness and 3D profile were measured using an Alicona Infinite Focus White light interferometry (WLI) and analysed using MountainLab software. A lateral resolution of $3 \mu\text{m}$ and vertical resolution of 50 nm was utilised. The surface was levelled to remove tilt, and waviness removed with a Robust Gaussian Filter and 0.25 mm cut off. Three roughness Ra, measurements were taken vertically and horizontally for each sample and averaged. The vertical and horizontal surface roughness were separate to isolate specific details of the laser process. The horizontal roughness (RaH) captured detail on the surface along the laser path. The vertical roughness (RaV) captured detail through laser passes, Fig. 1b. Various 3D roughness measures were taken using Abbott-Firestone's curve, but the Reduced peak height (Spk) was the measure of concern also known as the peak distribution on the surface. A high Spk implies that the surface has many peaks. The initial contact with another surface will cause most of the forces to be confined to these small peaks thus increasing the contact pressure. This leads to surfaces

quickly eroding and being worn down, a necessary consideration in cutting tools. This variable is also useful to know for the amount of area for lubricant retention and debris collection available. Scanning Electron Microscope (SEM), TM3030 Hitachi backscatter SE, was used to view the surface topography in particular to identify microstructure boundaries, cracks, thermal shock, voids, pores, splatter and balling as a result of laser processing. These defects affects the performance of a material in application [24]. Energy Dispersive Spectroscopy (EDS) analysis for chemical composition in various regions. The material removal has been calculated based on previous research [22].

2.4. Crack Analysis

A new method was developed to estimate crack density to characterise crack formation in laser treated specimens. Cracks were identified as regions of material separation distinctly different from other surface defects such as a splatter boundary that follows the molten material shape. Firstly, the cracks were classified into three categories: superficial cracks, micro-cracks, and deep cracks by SEM inspection of the samples. Superficial cracks were faint, hairline scratches (length up to 20 µm). Micro-cracks were thicker cracks or cracks longer than 20 µm (length up to 100 µm, width up to 3 µm). Deep cracks were cracks that caused significant damage/breakage or void-like failures (or length \geq 20 µm and width $>$ 3 µm). All the cracks in a 225 µm x175 µm sample space were outlined, categorised, and counted for each sample (Fig. 2).

The quantity of each in the area was scaled up to estimate the crack density of each type of crack present on a 1 mm² area, resulting in a crack density value for each type of crack. The crack characterisation extrapolation is a valid estimation as laser processing is well established for its repeatability and reliability [25]. The total number of cracks from each sample was then compared to the fluence and frequency settings used to process that sample, allowing for an ANOVA result to be computed. It was important to generate this technique to have a quantitative analysis of crack formation as there is currently no universal way of characterising cracks based on type. As this is a visual technique, the sample space used will be dependent on the workpiece material. It should be a size that covers at least 3 laser paths with the magnification set to view surface cracks to a good resolution. The crack classification is only relevant to surface inspection, the penetration and depth of cracks are out of scope. The length and measurement criterion is based on the works of Denkena et al. [26] which studied micro-crack formation in hard metal milling tools. The length of cracks is measured by overlaying a straight line from end to end for linear crack shapes. Cracks that deviated significantly from a linear shape were measured in segments.

Results

Surface roughness is a clear way of characterising the surface quality after processing. The as-received sample had an RaH 0.4628 µm, RaV 0.5585 µm and Spk 0.9033 µm. The gradient value from each parameter when moving from the -1 to 1 level (Table 2, by DOE) was calculated to evaluate the effects and interaction effects on the roughness values (Fig. 3, Table 5). For all three roughness parameters,

fluence had the greatest effect. An increase from 0.050 J/cm^2 to 0.149 J/cm^2 , caused an increase of $0.1203 \mu\text{m}$, $0.1644 \mu\text{m}$, $0.4189 \mu\text{m}$ for RaV, RaH and Spk respectively. For RaV, the interaction of frequency and speed was the next greatest effect. However, speed independently reduced the roughness, but frequency independently increased the roughness. The remaining effects are less contributory. RaH followed a different trend with frequency, the interaction of fluence and frequency and the interaction of fluence, frequency and feed speed having the most significant values. Hatch distance had less of an effect suggesting that the heat accumulation from other parameters is more likely to cause a poorer surface than having a smaller space between the laser passes.

Table 5
Parameters and interaction definitions.

Parameter	Effect of
Ψ	Fluence
f	Frequency
v	Feed speed
d	Hatch distance
$\Psi*f$	Interaction of fluence and frequency
$\Psi*v$	Interaction of fluence and feed speed
$\Psi*d$	Interaction of fluence and hatch distance
$f*v$	Interaction of frequency and feed speed
$f*d$	Interaction of frequency and hatch distance
$v*d$	Interaction of feed speed and hatch distance
$\Psi*f*v$	Interaction of fluence, frequency and feed speed
$\Psi*f*d$	Interaction of fluence, frequency and hatch distance
$\Psi*v*d$	Interaction of fluence, feed speed and hatch distance
$f*v*d$	Interaction of frequency, feed speed and hatch distance
$\Psi*f*v*d$	Interaction of fluence, frequency, feed speed and hatch distance

The factors that consistently reduced the roughness were speed, the interaction between fluence and speed, the interaction between frequency and speed and the interaction of fluence, frequency and feed speed; confirmed with the lack of defects on the microstructure on samples. This suggested that increasing the speed improved 2D and 3D surface roughness and when optimised with fluence and frequency, an even better result was achieved in terms of 2D and 3D roughness.

Table 6 shows the percentage variation of Spk from the as-received surface using Eq. (1). Experiments processed at a fluence of 0.050 J/cm^2 had a $\pm 20 \%$ variation from the as received.

$$\text{Percentage variation (\%)} = \left(\frac{(Spk \text{ value from test}) - (As - received Spk)}{As - received Spk} \right) \times 100 \quad (1)$$

Table 6
– Percentage variation of Spk form the as-received sample compared to each experiment.

Experiment	Ψ (J/cm ²)	f (kHz)	v (mm/s)	d (mm)	Percentage variation from as-received surface
0	0.099	35	1000	0.04	32%
1	0.050	17.5	500	0.02	23%
2	0.149	17.5	500	0.02	33%
3	0.050	52.5	500	0.02	11%
4	0.050	17.5	1500	0.02	1%
5	0.050	17.5	500	0.06	12%
6	0.149	52.5	500	0.02	140%
7	0.149	17.5	1500	0.02	78%
8	0.149	17.5	500	0.06	38%
9	0.050	52.5	1500	0.02	13%
10	0.050	52.5	500	0.06	7%
11	0.050	17.5	1500	0.06	5%
12	0.149	52.5	1500	0.02	50%
13	0.050	52.5	1500	0.06	16%
14	0.149	17.5	1500	0.06	45%
15	0.149	52.5	500	0.06	400%
16	0.149	52.5	1500	0.06	47%

The distribution of the Spk values is shown in Fig. 4. The lower fluence setting had a relatively small distribution compared to the higher setting; the mean is 43 % higher. Frequency followed a similar pattern where the lower setting had a much smaller distribution than the higher setting; and a 30 % increase in mean. The speed and hatch distance had a smaller difference and is distributed with the quartiles overlapping at the two levels. However, at a higher speed setting the deviation was within a 10 % variation of the as-received Spk value. Hatch distance had the least variational difference between the levels.

Pareto analysis or cumulative frequency (Fig. 5) was also conducted on the parameters and the interaction using absolute gradient values, to prioritise which parameters caused a greater change in roughness. Fluence had the highest contributory effect on all roughness variables and therefore is a

necessary factor to reduce the roughness and have a better surface homogeneity. In all roughness parameters, a variate of frequency and speed (or interaction) had the second greatest effect on the roughness; indicating that speed and frequency need to be viewed as linked parameters when considering surface roughness in both 2D and 3D parameters. Spk was affected by the interactive effects of parameters more where the interaction between fluence, speed and frequency and the interaction of frequency and speed had the next largest contribution to the Spk. This suggested the importance of considering parameters as related variables and not isolated.

Experiment 15 had the highest average Spk value and variation of 4.156 μm and 400% respectively. This is due to the energy transfer being very high in the areas that are directly exposed to the pulsed laser. These regions resulted in deep grooves on the surface with depth in the region of 10 μm . The larger hatch distance used in this experiment made the surface profile comparable to a textured surface with linear grooves (Fig. 6) hence the very high Spk value.

3.1. Surface roughness modelling

The main effects of each parameter were represented as a plot between the levels investigated (Fig. 7). The magnitude of each gradient indicated how sensitive each factor was to the Spk parameter.

DOE analysis generated the coefficients used to create the linear model in Eq. (2) with a minimised error percentage (1 %):

$$Spk_{Model} = 0.9033 + 0.41885\psi + 0.24755\psi f - 0.21025\psi v + 0.13255\psi d - 0.15635vd - 0.30205\psi fv \quad (2)$$

where ψ is fluence (kJ/m^2), f is frequency (MHz), v is speed (m/s), and d is hatch distance (mm). The parameters included in the equation aligns with the experimental data investigated in this study. For example, as the laser fluence increased the peak distribution on the surface increased. The higher energy caused more aggressive material melting on the surface leading to more molten material distribution and peaks. The model also takes the interaction effect of the other parameters to show how they limit or contribute to peaks on the surface. Figure 8 shows this model against the average Spk results measured from experimental data.

The model prioritised fluence and the interaction effects between frequency and speed shown in the previous analysis. It predicted the roughness in the melting region of laser processing with an accuracy of 69 %. Eduardo et al. [27] reported a similar accuracy when modelling the melted layer geometry from laser additive manufacturing in Inconel 625 and Iron. The Spk model performed best at moderate to medium level of processing (fluences in the region of 0.050–0.099 J/cm^2) with an error between 1 % to 10 %. The material removal was approximately less than 0.27 μm^3 . When the fluence was 0.149 J/cm^2 there was more violent material melting and expulsion; the material removal was higher than 0.40 μm^3 , approximately. The model failed to predict this behaviour accurately with the error percentage between 15 % to 36 %. This suggests that different models may be needed to fully model the transition from the melting phase to the boiling/vaporisation phase. This is not an uncommon result when studies have

attempted to model the laser process. Volpe et al. [28] created a predictive model for the femtosecond laser micro-milling on acrylic (PMMA). The linear model described most of the results but required adaptation using regression was needed to cause certain settings to fall within a good confidence level. Schatz and Patel [29] also found this with DOE modelling of pulsed laser deposition on lead zirconate titanate (PZT) thin films. Multiple models were generated but no one model perfectly fell within a good confidence level but concluded that power and pressure were the most influential factors on the PZT properties.

Fluence caused more melting on the surface and melt redistribution, which increased the chance of microstructural changes and poorer surface. As the cooling rate was not controlled, the solidification rate varied in different regions. Some areas experienced faster cooling leaving small grains and some areas slower cooling leaving larger grains. The mixture of these rate caused voids, porosity and transitional boundaries characterised by peaks on the surface. The trends shown with these parameters are in line with the current material science of laser processing. Davoren et al. [5] studied laser net-shaping WC-9.2Ni with a fibre laser with powers ranging from 150–350 W. A higher power caused a larger molten pool, resulting in a greater change in the microstructure. This created areas of different morphologies of spheroids and fish-bone structures, close to the processed area. Xiong et al. [30] presented similar results when laser net-shaping WC-Co, where a higher power created a greater variation in WC particle size causing voids and porosity. There was also a larger HAZ in the surrounding region.

The results of the study concluded that fluence is the most influential factor on surface peak generation. The higher energy caused more aggressive material processing and redistribution. This highlighted that fluence is a necessary factor to be optimised to minimise the roughness and have better surface homogeneity overall. The interaction effects of parameters were also significant, indicating that the surface quality cannot solely be optimised using one parameter and parameters cannot be looked at independently. The interaction of fluence and frequency and the interaction of speed and frequency should be considered correlated. A faster speed reduced the number of thermal defects present. However, the frequency had a greater effect on crack formation and the types of cracks formed.

3.2. Surface crack optimisation

Cracks are detrimental to the surface integrity and mechanical properties of WC post laser processing (Khmyrov et al. [31]) (Paul et al. [8]). In this paper, a micro-crack classification system was developed, and a crack density variable was introduced to estimate cracks and crack type on a 1 mm^2 area size. Fluence and frequency settings were investigated to isolate these parameters against the crack formation. With a constant feed speed and hatch distance, fluence and frequency settings were investigated between 0.05–0.20 J/cm^2 and 5–100 kHz respectively (Table 4). Figure 9 shows the result of the crack density distribution and Fig. 10 shows instances of each type of crack at various processing settings. The crack density increased as the fluence increased but peaks at 0.099 J/cm^2 for most frequency settings. Deep cracks were signs of significant damage in the area, on average they did not present until 40 kHz and were situated around balling and splatter defects. Deep cracks were present mostly above 0.099 J/cm^2 .

across the frequency settings. Micro-cracks were mainly present with the lower fluence settings across the range of frequencies, around the main laser track path area. They were more likely to form between 0.050–0.135 J/cm². Superficial cracks were present in all frequency settings but particularly with lower fluence settings. This crack type was highest at 0.070 J/cm² and 35 kHz. The crack density of each crack type increased between 0.050–0.099 J/cm² across all frequency settings then decreased as the fluence increased to 0.20J/cm².

The transition to thermal shock fracturing can be seen at 0.099 J/cm² where there was an equal distribution of the crack types. The lowest density of all three cracks types occurred at 0.149 J/cm² fluence and 52.5 kHz, the microstructure showed a good amount of melting, uniform material processing and resolidification (Fig. 11a). Overall, these results suggested that there was a link between crack defects formation and the variation of fluence and frequency.

The types of cracks identified on the samples loosely followed a pattern. Superficial cracks were randomly distributed throughout the sample, in no specific regions or areas. Micro-cracks mainly presented within the main laser track area i.e., along the RaH profile. Deep cracks were found in the overlapping laser track regions. Figure 11b generally shows this crack distribution.

The cracking behaviour of the material was investigated using ANOVA and the crack density variable to against fluence and frequency. Table 7 shows the results of this analysis to provide an understanding of the crack formation mechanism based on fluence and frequency. The sample size included 147 specimens. The magnitude of the f-statistics paired with a low p-value less than 0.1 (10 % significance level) indicated that fluence and frequency independently had a considerable effect on the crack density. Fluence had a greater contributory magnitude. However, the interaction of fluence and frequency was not a substantial effect in crack density. The outcome of this analysis showed that crack generation can be altered by specific laser parameters. Future work should investigate the refinement of the fluence setting to reduce crack formation and subsequently frequency to quantify a threshold based on WC composition and relative laser system setups. The results showed that there was sufficient evidence to support the claim that crack formation can be altered by fluence and frequency independently, but it is not dependent on the interaction of both. This is the first time cracks have been analysed with the statistical process in the laser processing of WC.

Table 7
ANOVA results for crack density using Fluence and Frequency.

Source	Type III Sum of Squares	df	Mean Square	f-statistic	p-value
Fluence	8492.892	2	4246.446	6.493	0.004
Frequency	3930.630	2	1965.315	3.005	0.061
Frequency * Fluence	1906.973	4	476.743	0.729	0.578
a. R Squared = .352 (Adjusted R Squared = .222)					

Discussion

The as-received microstructure had a highly homogeneous crystallinity, Fig. 12. Experiments referenced in this section refer to Table 3. The processed samples showed different levels of discoloration, samples processed at 0.149 J/cm^2 and 52.5 kHz had noticeable regions of darker regions indicative of burning. In these regions, there was a high percentage of carbon (Table 8), possibly due to the high energy causing material disassociation on the sample (Fig. 13). This is an effect when WC is exposed to high temperatures, causing the carbon in the WC phases to diffuse into the binder phases [35]. For example, Chen et al. [36] found this in the laser additive manufacturing of WC-reinforced iron and Bartkowski et al. [37] noticed this effect when laser cladding Fe/WC on low carbon steel.

Table 8 - Chemical composition at burnt regions within samples.

Element	C	O	Co	W	Al	Si
wt%	50.5	16.7	7.5	22.3	0.3	2.0

Majority of the samples had a distinct HAZ around the 1 mm^2 processing region, with a border of approximately 0.25 mm; this is expected as carbides often suffer from HAZ to different degrees depending on the processing parameters. Dumitru et al. [13] explained this is due to the small optical penetration depth of WC, which causes heat diffusion in the laser processing area. The microstructure of the laser treated surfaces indicated that temperature was too low for the surface to properly melt all phases of the material [32], [33]. The binder and WC phase were thermally excited to different extents due to the difference in thermal properties within the material (Table 9 [34]). This resulted in the array of cracks throughout the surface by the expansion and contraction of the binder.

Table 9 - Thermal properties of materials associated with Tungsten Carbide.

	WC	Co
Thermal conductivity (α_1), $\text{Wm}^{-1}\text{K}^{-1}$	110	100
Thermal expansion coefficient (κ), μK^{-1}	5.5	13

4.1 Effect of fluence and speed on material processing

Fluences above 0.099 J/cm^2 resulted in a significantly changed microstructure where there was a lot of molten material redistribution. This is caused by the photon momentum of the process [38] – causing a splatter/splotchy geometry, these features had a diameter of around $45 \mu\text{m}$ (Fig. 14a).

The ridges surrounding the circular geometries explained the increase of peaks and valleys on the surface. Analytically fluence had the greatest effect on peaks on the surface; this is also the case on a microstructural level. When comparing all the samples that were processed at 0.149 J/cm^2 , they had a resembling microstructure despite changing the other parameters. This indicated that there was a fluence threshold, between 0.099 J/cm^2 and 0.149 J/cm^2 on the WC structure, above which fluence dictated the resulting microstructure. All the experiments processed at 0.050 J/cm^2 had greater variation in appearance and surface morphology suggesting other parameters take precedent on the resultant microstructure.

Experiments processed with 0.149 J/cm^2 , 52.5 kHz and 500 mm/s transferred the most amount of laser energy; they appeared burnt and had the most remelting in the region, Fig. 14b, Fig. 14d. This is as expected as the high fluence and frequency paired with the slower speed prolonged the amount of energy delivered – giving time for the workpiece to heat and melt but not ablate [39] [13]. In some samples, the laser raster pattern was evidenced by material peaks and bulges of remelted material, Fig. 14e. The effect of fluence on the surface topography is shown in Fig. 15. The 0.149 J/cm^2 fluence caused more melting, with material migration resolidified on the surface giving the splatter like appearance referred to before. There were also fewer cracks, transverse to the laser beam path. Marimuthu et al. [1] found a similar trend when using picosecond laser to process WC. As the fluence increased the material removal and crater roughness increased, however less cracking damage was present in the surrounding microstructure. The 0.050 J/cm^2 samples exhibited smaller circular regions of melt expulsion and voids with a greater distribution of cracks.

Increasing the speed showed a clear improvement in the quality of surfaces. Speed dictated how long each area of the workpiece was exposed to the laser and changed the amount of energy deposited. A slower speed increased the amount of thermal damage to the surface giving rise to a range of defects. The samples processed with the faster speed of 1500 mm/s had a more homogeneous surface in relation to uniformity and the distribution of defects. This was attributed to the laser energy causing localised heating and the momentum of the process distributing molten material causing splatter to spread through multiple laser tracks (Fig. 16b). A slower speed concentrated more heat in specific areas, giving rise to even more splatter and localised defects (Fig. 16a).

Speed also altered the general response of the material to the laser. Experiment 3 showed significant thermal shock evidenced by numerous superficial and micro-cracks (Fig. 17). This was a result of the slow speed and higher frequency combination, as other samples processed with 500 mm/s and 17.5 kHz also presented a similar crack distribution. The WC grades used in this study had a relatively low WC content with a greater presence of the cobalt binder. As the WC and binder have very different thermal expansion coefficients, $5.5 \mu\text{K}^{-1}$ and $13 \mu\text{K}^{-1}$ respectively; each constituent expands at a different rate causing internal stresses and cracks. This was also demonstrated in the SLS of WC-Co by Paul et al. [8], where the rapid cooling of the cobalt phase caused high surface tensions in the molten pool. This caused cracks and geometric distortions. A higher weight percentage of WC would reduce this effect if the same parameters were used as less of the binder would be present to induce stresses [24]. Khmyrov et al. [31] showed this when laser sintering WC-Co of equal weight percentages, and found many cracks due to the formation of $\text{W}_3\text{Co}_3\text{C}$ brittle phases.

A further look into speed on the material processing was done using the 0.050 J/cm^2 to limit the effect of fluence on the surface (Fig. 18).

At slower speed there a greater build-up of heat allowed for greater energy transfer. This increased the likelihood of the thermal mismatch, which presented as cracks and voids particularly at the carbide/binder interface [6]. At 250 mm/s, cracks were concentrated and prevalent near voids (Fig. 19). As the speed increased there was more irregular heating causing porosity (Fig. 19). At 750 mm/s the voids became larger and more frequent on the surface (Fig. 20). The fastest speed of 2500 mm/s exhibited regions of barely processed areas surrounded by porosity (Fig. 21); from the non-uniform heating and rapid solidification, restricting the material's ability to melt and remelt uniformly [40].

4.2 Effect of frequency on the fracture mechanism

Frequency affected the amount of energy the laser transferred to the surface, the higher the frequency the greater the potential heating effect. Previous analysis showed that frequency was a clear factor in crack formation on the surface [8]. As frequency had such a dramatic effect on the surface, a further inquiry into material response was conducted. Figure 22 shows the result using higher frequency levels. SEM analysis showed that thermal excitation at the high frequency changed the material response to crack generation.

At the lowest frequency of 5 kHz there was a heterogenous energy distribution demonstrated by the clear regions of material transition, similar to when a large hatch distance is used (Fig. 22a). The boundary laser regions and overlapping tracks was characterised by voids, balling, and irregular pores (Fig. 23). At 17.5 kHz, the surface showed more mechanical effects of cracking; with time for molten material to distribute (Fig. 22b). The thermal response from the laser, from 40 kHz, began to dominate the morphological changes, altering the characteristics of the cracks and defects balling became more pronounced and frequent (Fig. 24); caused by Marangoni convections from the higher temperature gradient. This caused the material to solidify before spreading along the surface. This phenomenon has mainly been found in SLS. Zhou et al. [41] studied the balling of pure tungsten with SLS by changing the

laser exposure time. A longer laser exposure time caused thermal convection currents in the molten pool making the balling more distinct and larger. This balling defect has also been present in other materials. Khairallah et al. [42] investigated the physics of laser powder bed fusion of stainless steel and found that the balling effect is a result of the surface tensions. The balling was minimised by controlling the heat concentration on the laser processed area. From 52.5 kHz, a greater heat accumulation in the surface caused more remelting and splatter like regions. The movement of splatter was also confined to the width of the laser track indicating insufficient time to distribute around the surface (Fig. 22e). The 100 kHz frequency setting had a distinct surface morphology, with fewer defects of balling and spherical pores (Fig. 25). It was evident from this that there was a progressive transition from mechanically induced stress from the laser to a thermally driven response. This trend has also been seen in the laser processing of gold alloy thin films by Geremia et al. [43].

Conclusion

The presented findings show an initial insight understanding the surface integrity of laser surface engineered tungsten carbide. The material response to different laser process parameters (fluence, frequency, speed, and hatch distance) was evaluated, using a pulsed fibre laser at 1060 nm wavelength in the ns regime pulse duration. The conclusions are summarised:

- Both mechanical and thermal effects arise from laser processing e.g., fracturing and melting, respectively.
- In this paper a crack classification system and a crack density variable were introduced to estimate the number of cracks and crack type within a 1 mm^2 area size. The analysis found that fluence and frequency have a significant effect on the crack density independently but not the interaction of both. The crack density increased between $0.050\text{--}0.099\text{ J/cm}^2$ across all frequency settings then decreased as the fluence increased to 0.20 J/cm^2 . Superficial cracks were present in all frequency settings but particularly with lower fluence settings. Micro-cracks were more likely to form between $0.050\text{--}0.135\text{ J/cm}^2$. Deep cracks did not present until 40 kHz or above 0.099 J/cm^2 across the frequency settings.
- A linear model to predict surface roughness was proposed. It performed best when there was a moderate to medium level of processing, with an error between 1–10 %; but failed to accurately model the behaviour when there was more violent material melting, with an error between 15–36 %. It can be concluded that the interaction of parameters is as important to optimise as the parameters themselves independently. This process showed the laser process can be modelled however different models may be required to describe the behaviour at different processing states i.e., melting or ablation.
- To build more confidence in the robustness of optimisation more advanced modelling techniques will be considered including artificial intelligence (AI) and deep learning. These methods can handle a greater number of parameters and settings to analyse the surface integrity. AI processing can also aid in inspecting surface cracks with visual inspection techniques. The aim of study was to develop

a method to understand and control the laser processing of brittle materials to retain the surface integrity for various applications.

Declarations

Ethical Approval

Not applicable

Consent to Participate

Not applicable

Consent to Publish

All authors have reached agreement for publication.

Authors Contributions

All authors contributed to the work with the order provided.

Funding

The research leading to these results received funding from the Manufacturing Technology Centre (MTC) in support of the PhD studentship.

Competing interests

The authors have no conflicts of interest to declare that are relevant to the content of this article.

Availability of data and material

Not applicable

Corresponding author

Correspondence to Manuela Pacella.

Acknowledgments

The authors would like to acknowledge the Manufacturing Technology Centre for their financial support to the Ph.D. project, and the assistance of Shaun Fowler in the Loughborough Materials Characterisation Centre.

References

- [1] S. Marimuthu, J. Dunleavey, and B. Smith, "Picosecond laser machining of tungsten carbide," *Int. J. Refract. Met. Hard Mater.*, vol. 92, no. January, p. 105338, 2020, doi: 10.1016/j.ijrmhm.2020.105338.
- [2] G. T. Smith, *Cutting Tool Technology*. London: Springer London, 2008.
- [3] M. Pacella, "A new low-feed chip breaking tool and its effect on chip morphology," *Int. J. Adv. Manuf. Technol.*, vol. 104, no. 1–4, pp. 1145–1157, 2019, doi: 10.1007/s00170-019-03961-2.
- [4] P. Schwarzkopf, R. Kieffer, W. Leszynski, and F. Benesovsky, *Cemented Carbides*. The Macmillan Company, 1960.
- [5] B. Davoren, N. Sacks, and M. Theron, "Laser engineered net shaping of WC-9.2wt%Ni alloys: A feasibility study," *Int. J. Refract. Met. Hard Mater.*, vol. 86, no. June 2019, p. 105136, 2020, doi: 10.1016/j.ijrmhm.2019.105136.
- [6] L. S. Sigl and H. E. Exner, "EXPERIMENTAL STUDY OF THE MECHANICS OF FRACTURE IN WC-Co ALLOYS," *Metall. Trans. A, Phys. Metall. Mater. Sci.*, vol. 18 A, no. 7, pp. 1299–1308, 1987, doi: 10.1007/BF02647199.
- [7] S. Herd, R. J. K. Wood, J. A. Wharton, and C. F. Higgs, "Explicit fracture modelling of cemented tungsten carbide (WC-Co) at the mesoscale," *Mater. Sci. Eng. A*, vol. 712, no. May 2017, pp. 521–530, 2018, doi: 10.1016/j.msea.2017.11.109.
- [8] S. Paul, R. Singh, and W. Yan, "Lasers Based Manufacturing," no. June 2016, 2015, doi: 10.1007/978-81-322-2352-8.
- [9] Z. Wu, "The mechanism governing cutting of hard materials with hybrid Laser / Waterjet system through controlled fracture," 2015.
- [10] C. Lee, H. Park, J. Yoo, C. Lee, W. Woo, and S. Park, "Residual stress and crack initiation in laser clad composite layer with Co-based alloy and WC + NiCr," *Appl. Surf. Sci.*, 2015, doi: 10.1016/j.apsusc.2015.03.168.
- [11] D. P. H. HASSELMAN, "Unified Theory of Thermal Shock Fracture Initiation and Crack Propagation in Brittle Ceramics," *J. Am. Ceram. Soc.*, vol. 52, no. 11, pp. 600–604, 1969, doi: 10.1111/j.1151-2916.1969.tb15848.x.

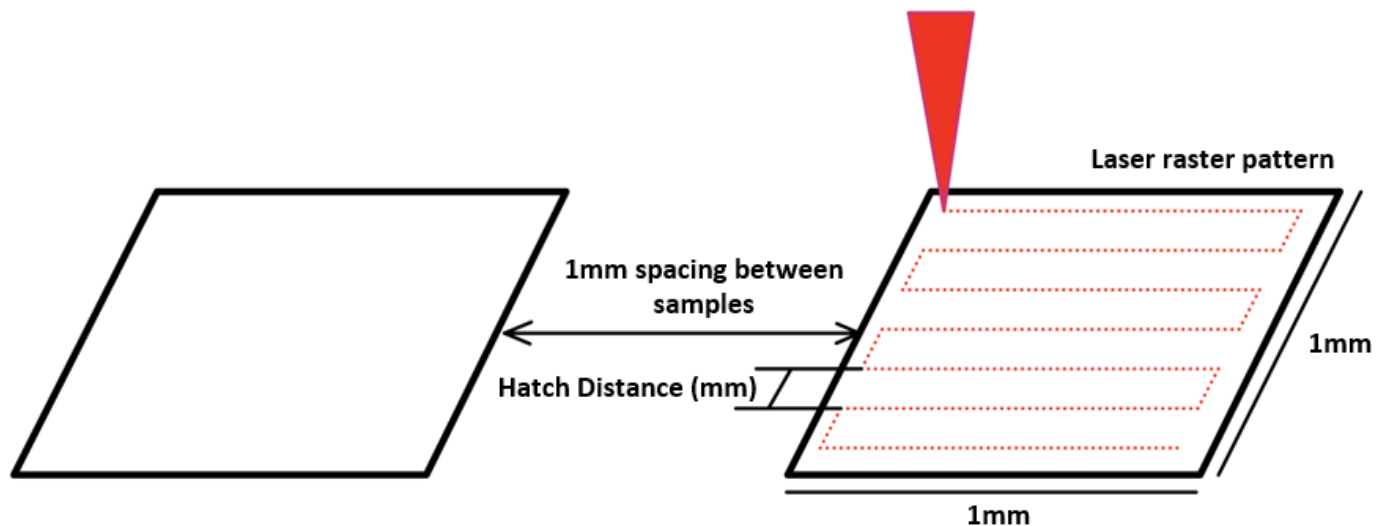
- [12] B. Wang, Z. Wang, J. Yuan, Z. Yin, L. Huang, and K. Zheng, "High temperature fracture mechanism of ultrafine WC-Co cemented carbides containing (Ti,W)C," *Int. J. Refract. Met. Hard Mater.*, no. xxxx, p. 105428, 2020, doi: 10.1016/j.ijrmhm.2020.105428.
- [13] G. Dumitru, V. Romano, H. P. Weber, M. Sentis, and W. Marine, "Femtosecond ablation of ultrahard materials," *Appl. Phys. A Mater. Sci. Process.*, vol. 74, no. 6, pp. 729–739, 2002, doi: 10.1007/s003390101183.
- [14] P. Lickschat, D. Metzner, and S. Weißmantel, "Fundamental investigations of ultrashort pulsed laser ablation on stainless steel and cemented tungsten carbide," *Int. J. Adv. Manuf. Technol.*, vol. 109, no. 3–4, pp. 1167–1175, 2020, doi: 10.1007/s00170-020-05502-8.
- [15] A. Ditsche and T. Seefeld, "Agglomerated tungsten carbide: A new approach for tool surface reinforcement," *Key Eng. Mater.*, vol. 809 KEM, pp. 121–127, 2019, doi: 10.4028/www.scientific.net/KEM.809.121.
- [16] Y. Wang, P. Molian, and P. Shrotriya, "Crack separation mechanism in CO₂ laser machining of thick polycrystalline cubic boron nitride tool blanks," *Int. J. Adv. Manuf. Technol.*, vol. 70, no. 5–8, pp. 1009–1022, 2014, doi: 10.1007/s00170-013-5312-3.
- [17] M. Pacella, V. Nekouie, and A. Badiee, "Surface engineering of ultra-hard polycrystalline structures using a nanosecond Yb fibre laser: Effect of process parameters on microstructure, hardness and surface finish," *J. Mater. Process. Technol.*, vol. 266, no. June 2018, pp. 311–328, 2019, doi: 10.1016/j.jmatprotec.2018.11.014.
- [18] B. Karpuschewski, K. Schmidt, J. Prilukova, J. Beňo, I. Maňková, and N. T. Hieu, "Influence of tool edge preparation on performance of ceramic tool inserts when hard turning," *J. Mater. Process. Technol.*, vol. 213, no. 11, pp. 1978–1988, 2013, doi: 10.1016/j.jmatprotec.2013.05.016.
- [19] E. Kacar *et al.*, "Characterization of the drilling alumina ceramic using Nd:YAG pulsed laser," *J. Mater. Process. Technol.*, vol. 209, no. 4, pp. 2008–2014, 2009, doi: 10.1016/j.jmatprotec.2008.04.049.
- [20] J. P. Calderón Urbina, C. Daniel, and C. Emmelmann, "Experimental and analytical investigation of cemented tungsten carbide ultra-short pulse laser ablation," *Phys. Procedia*, vol. 41, pp. 752–758, 2013, doi: 10.1016/j.phpro.2013.03.144.
- [21] T. L. See *et al.*, "Effect of geometry measurements on characteristics of femtosecond laser ablation of HR4 nickel alloy," *Opt. Lasers Eng.*, vol. 64, pp. 71–78, 2015, doi: 10.1016/j.optlaseng.2014.07.011.
- [22] M. Pacella, D. A. Axinte, P. W. Butler-Smith, and M. Daine, "On the topographical/chemical analysis of polycrystalline diamond pulsed laser ablated surfaces," *Procedia CIRP*, vol. 13, pp. 387–392, 2014, doi: 10.1016/j.procir.2014.04.066.

- [23] N. B. Dahotre and S. Harimkar, *Laser Fabrication and Machining of Materials*, Illustrate. Springer Science & Business Media, 2008.
- [24] T. Klünsner, T. Lube, C. Gettinger, L. Walch, and R. Pippan, "Influence of WC-Co hard metal microstructure on defect density, initiation and propagation kinetics of fatigue cracks starting at intrinsic and artificial defects under a negative stress ratio," *Acta Mater.*, vol. 188, pp. 30–39, 2020, doi: 10.1016/j.actamat.2020.01.057.
- [25] S. Mishra and V. Yadava, "Laser Beam MicroMachining (LBMM) - A review," *Opt. Lasers Eng.*, vol. 73, pp. 89–122, 2015, doi: 10.1016/j.optlaseng.2015.03.017.
- [26] B. Denkena, T. Grove, and M. Theuer, "Micro crack formation in hardmetal milling tools," *Int. J. Refract. Met. Hard Mater.*, vol. 70, no. October 2017, pp. 210–214, 2018, doi: 10.1016/j.ijrmhm.2017.10.008.
- [27] L. Eduardo, H. Santos, M. Pereira, W. Lindolfo, and L. Oliveira, "Surface & Coatings Technology Modeling layer geometry in directed energy deposition with laser for additive manufacturing," vol. 409, no. November 2020, 2021, doi: 10.1016/j.surfcoat.2021.126897.
- [28] A. Volpe, G. Trotta, U. Krishnan, and A. Ancona, "Prediction model of the depth of the femtosecond laser micro-milling of PMMA," *Opt. Laser Technol.*, vol. 120, no. August, p. 105713, 2019, doi: 10.1016/j.optlastec.2019.105713.
- [29] A. Schatz, D. Pantel, and T. Hanemann, "Application of DoE methods to establish a model for the pulsed laser deposition of PZT thin-films," *2016 Jt. IEEE Int. Symp. Appl. Ferroelectr. Eur. Conf. Appl. Polar Dielectr. Piezoelectric Force Microsc. Work. ISAF/ECAPD/PFM 2016*, pp. 2–5, 2016, doi: 10.1109/ISAF.2016.7578062.
- [30] Y. Xiong, J. E. Smugeresky, and J. M. Schoenung, "The influence of working distance on laser deposited WC-Co," *J. Mater. Process. Technol.*, vol. 209, no. 10, pp. 4935–4941, 2009, doi: 10.1016/j.jmatprotec.2009.01.016.
- [31] R. S. Khmyrov, V. A. Safronov, and A. V. Gusarov, "Obtaining crack-free WC-Co alloys by selective laser melting," *Phys. Procedia*, vol. 83, pp. 874–881, 2016, doi: 10.1016/j.phpro.2016.08.091.
- [32] V. N. Lednev *et al.*, "Sample temperature effect on laser ablation and analytical capabilities of laser induced breakdown spectroscopy," *J. Anal. At. Spectrom.*, vol. 34, no. 3, pp. 607–615, 2019, doi: 10.1039/c8ja00348c.
- [33] P. P. Shukla and J. Lawrence, "Fracture toughness modification by using a fibre laser surface treatment of a silicon nitride engineering ceramic," in *Journal of Materials Science*, Dec. 2010, vol. 45, no. 23, pp. 6540–6555, doi: 10.1007/s10853-010-4743-6.

- [34] Wolfram, "Thermal Expansion of the elements," 2020.
<https://periodictable.com/Properties/A/ThermalExpansion.html> (accessed Dec. 14, 2020).
- [35] C. Element and S. Technologies, "the Element Six."
- [36] H. Chen *et al.*, "Achieving high strength and high ductility in WC-reinforced iron-based composites by laser additive manufacturing," *Addit. Manuf.*, vol. 35, no. March, p. 101195, 2020, doi: 10.1016/j.addma.2020.101195.
- [37] D. Bartkowski, A. Bartkowska, and P. Jurčí, "Laser cladding process of Fe/WC metal matrix composite coatings on low carbon steel using Yb: YAG disk laser," *Opt. Laser Technol.*, vol. 136, no. August 2020, 2021, doi: 10.1016/j.optlastec.2020.106784.
- [38] R. D. Schaeffer, *Fundamentals of Laser Micromachining*. Danvers: Taylor & Francis, 2012.
- [39] P. Muthuswamy, "Additive Manufacturing of Tungsten Carbide Hardmetal Parts by Selective Laser Melting (SLM), Selective Laser Sintering (SLS) and Binder Jet 3D Printing (BJ3DP) Techniques," *Lasers Manuf. Mater. Process.*, vol. 7, no. 3, pp. 338–371, 2020, doi: 10.1007/s40516-020-00124-0.
- [40] R. S. Khmyrov, V. A. Safronov, and A. V. Gusarov, "Synthesis of Nanostructured WC-Co Hardmetal by Selective Laser Melting," *Procedia IUTAM*, vol. 23, pp. 114–119, 2017, doi: 10.1016/j.piutam.2017.06.011.
- [41] X. Zhou, X. Liu, D. Zhang, Z. Shen, and W. Liu, "Balling phenomena in selective laser melted tungsten," *J. Mater. Process. Technol.*, vol. 222, pp. 33–42, 2015, doi: 10.1016/j.jmatprotec.2015.02.032.
- [42] S. A. Khairallah, A. T. Anderson, A. Rubenchik, and W. E. King, "Laser powder-bed fusion additive manufacturing: Physics of complex melt flow and formation mechanisms of pores, spatter, and denudation zones," *Acta Mater.*, vol. 108, pp. 36–45, 2016, doi: 10.1016/j.actamat.2016.02.014.
- [43] R. Geremia, D. Karnakis, and D. P. Hand, "The role of laser pulse overlap in ultrafast thin film structuring applications," *Appl. Phys. A Mater. Sci. Process.*, vol. 124, no. 9, pp. 1–8, 2018, doi: 10.1007/s00339-018-2045-z.

Figures

a)



b)

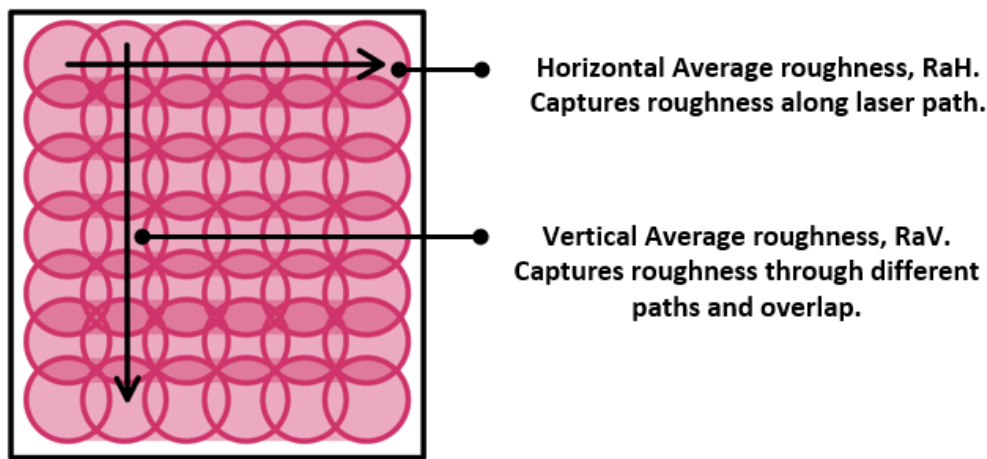


Figure 1

a) Laser raster pattern, b) 2D Average roughness parameters in the vertical and horizontal direction.

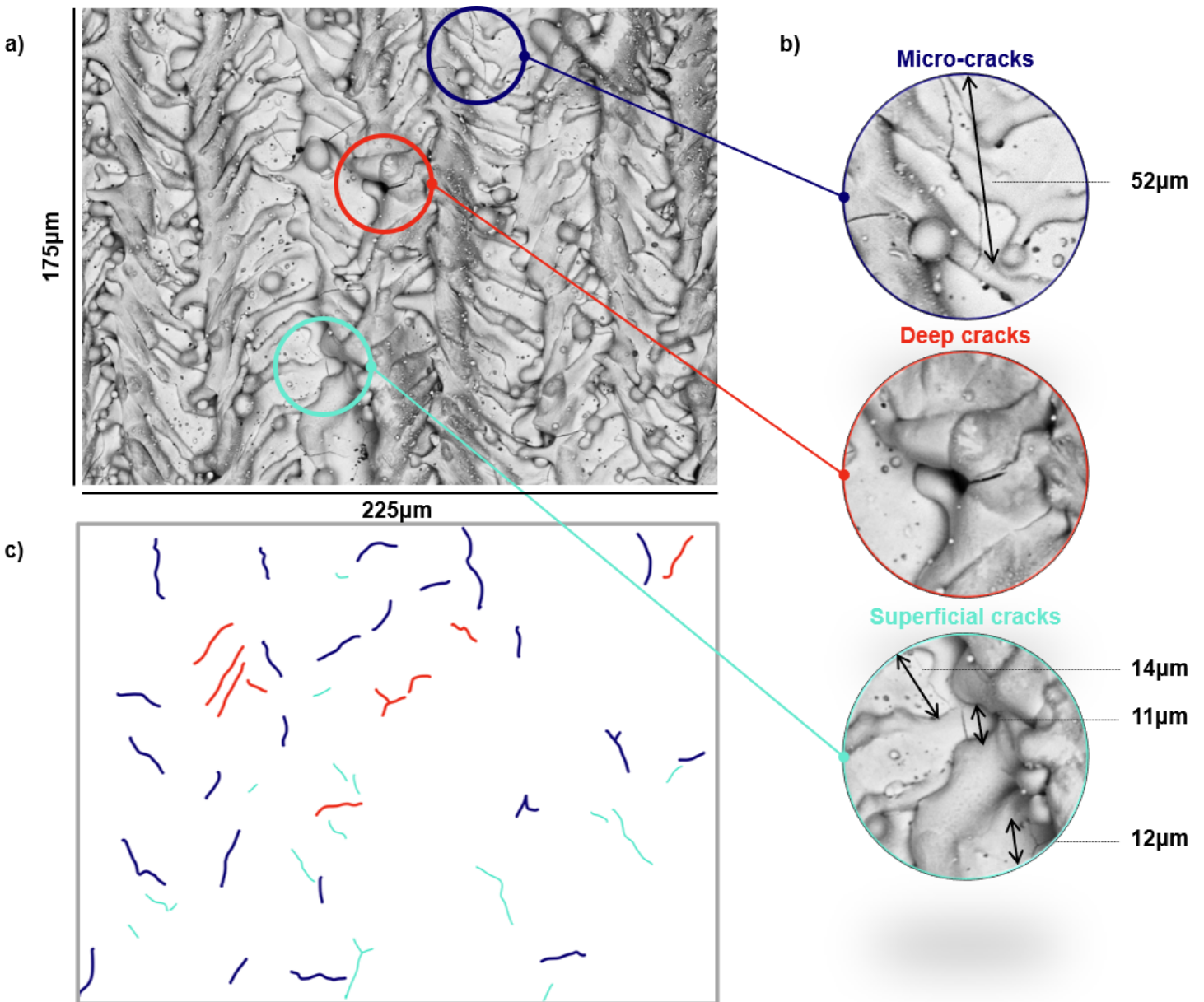


Figure 2

a) Example of sample size for crack analysis, b) examples of crack categorisation based on size and damage to surface, c) representation of each type of crack from a sample.

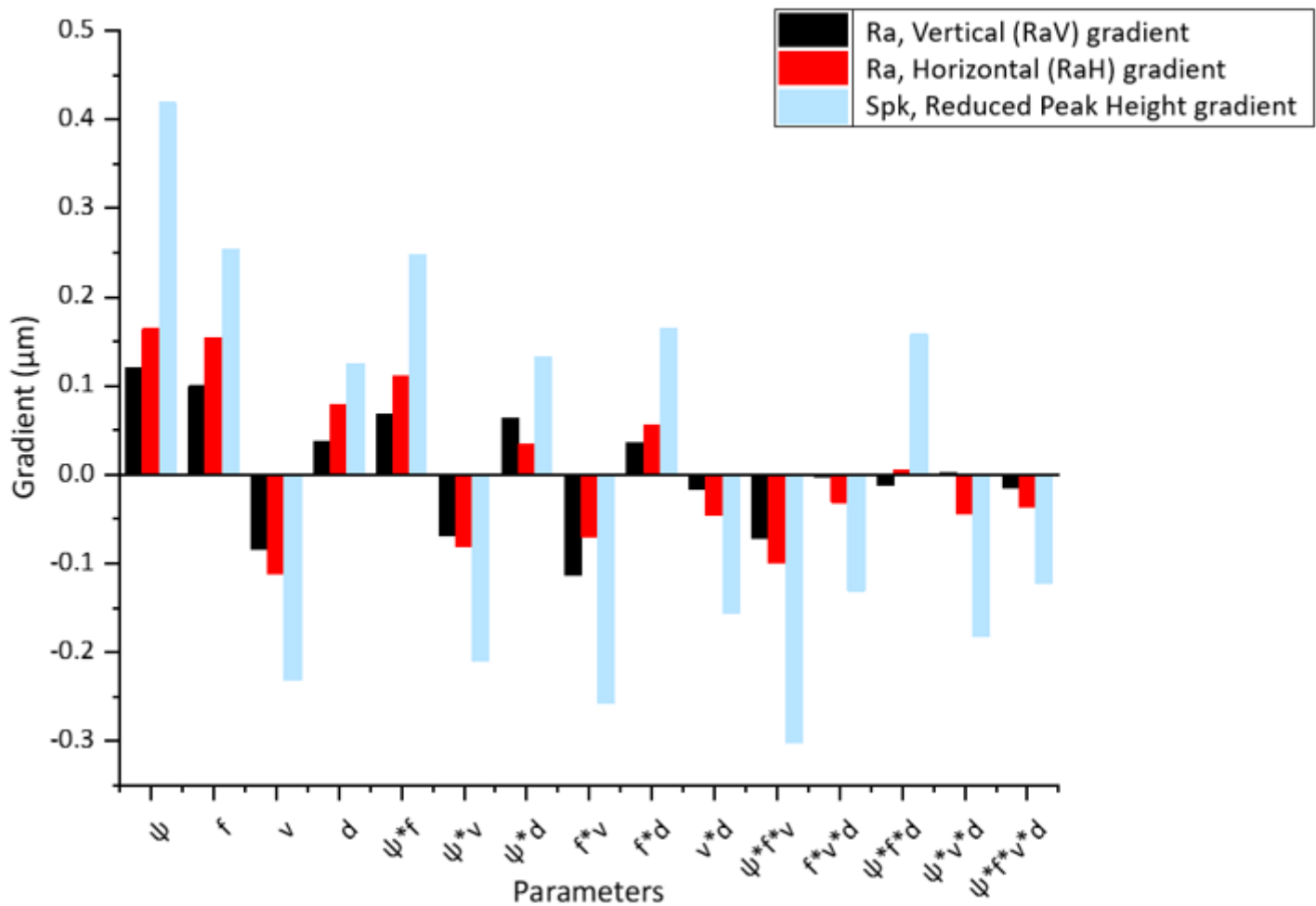


Figure 3

Gradient values of moving from each level for each parameter.

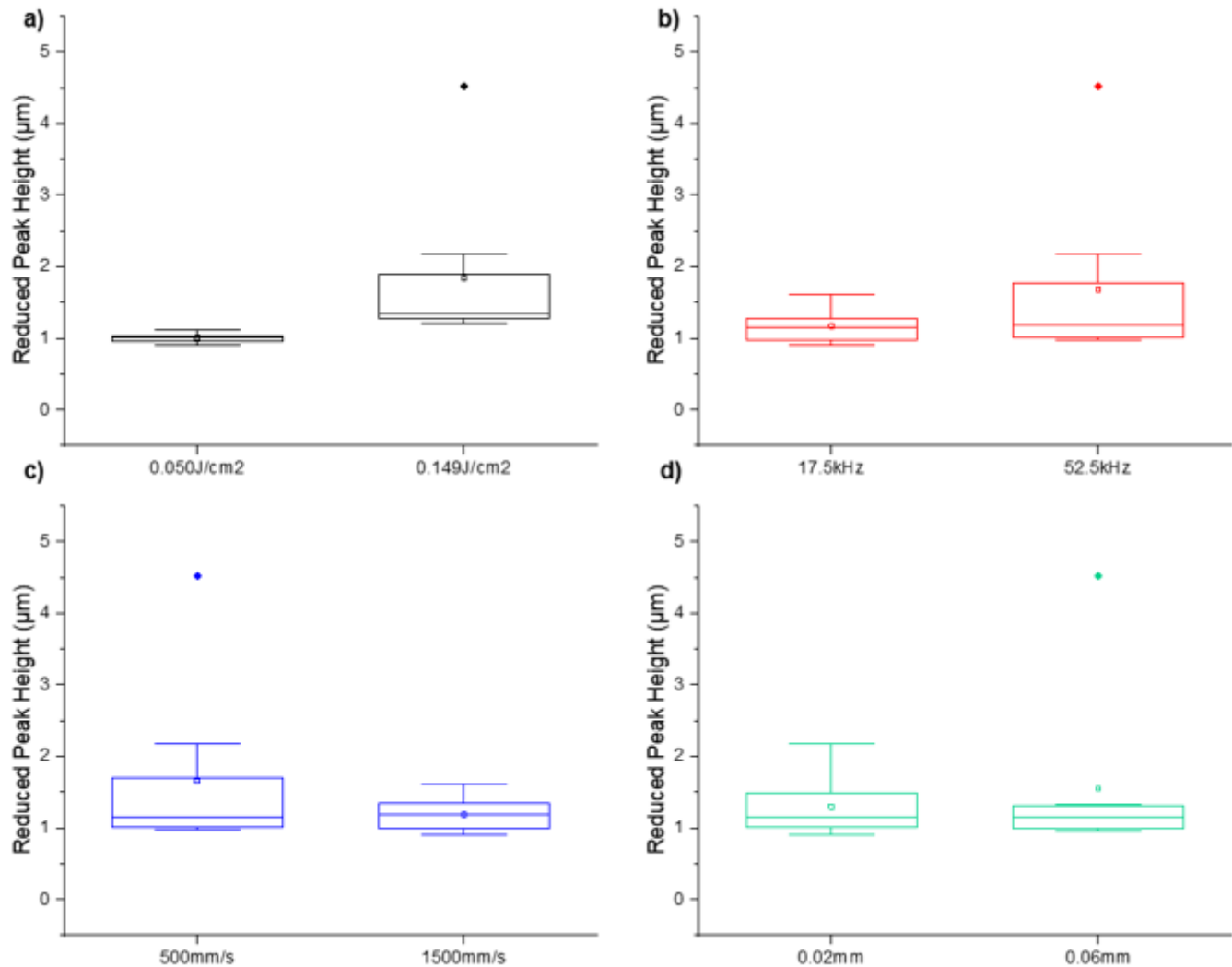


Figure 4

Box plot of Spk for a) Fluence, b) Frequency, c) Speed and d) Hatch distance.

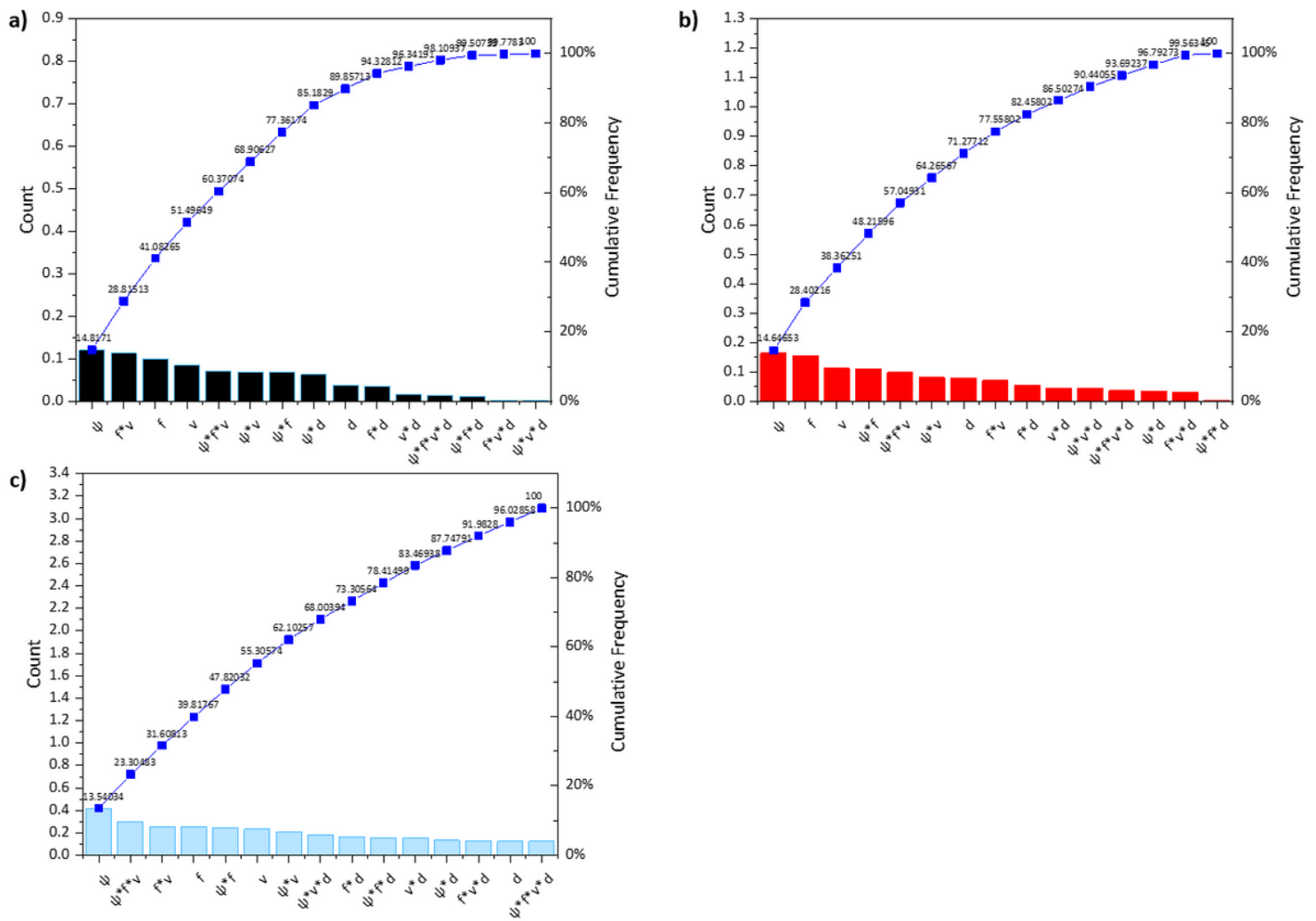


Figure 5

Pareto effect of each roughness variable based on the parameters chosen. a) RaV – Vertical average roughness, b) RaH – Horizontal average roughness, c) Spk – Reduced Peak Height.

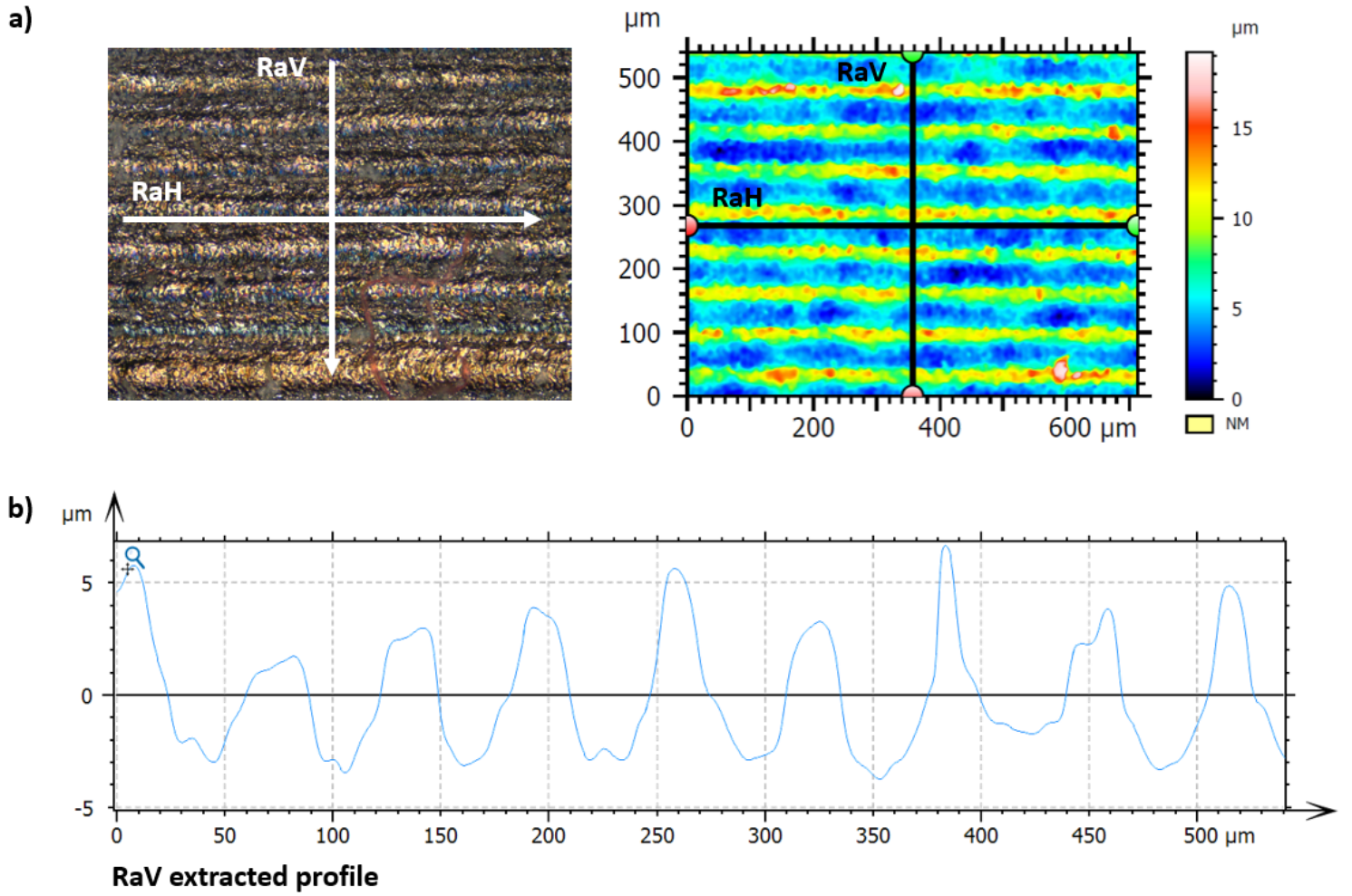


Figure 6

a) Roughness profile direction on Experiment 15, b) RaV 2D surface roughness profile for Experiment 15 of 24 design.

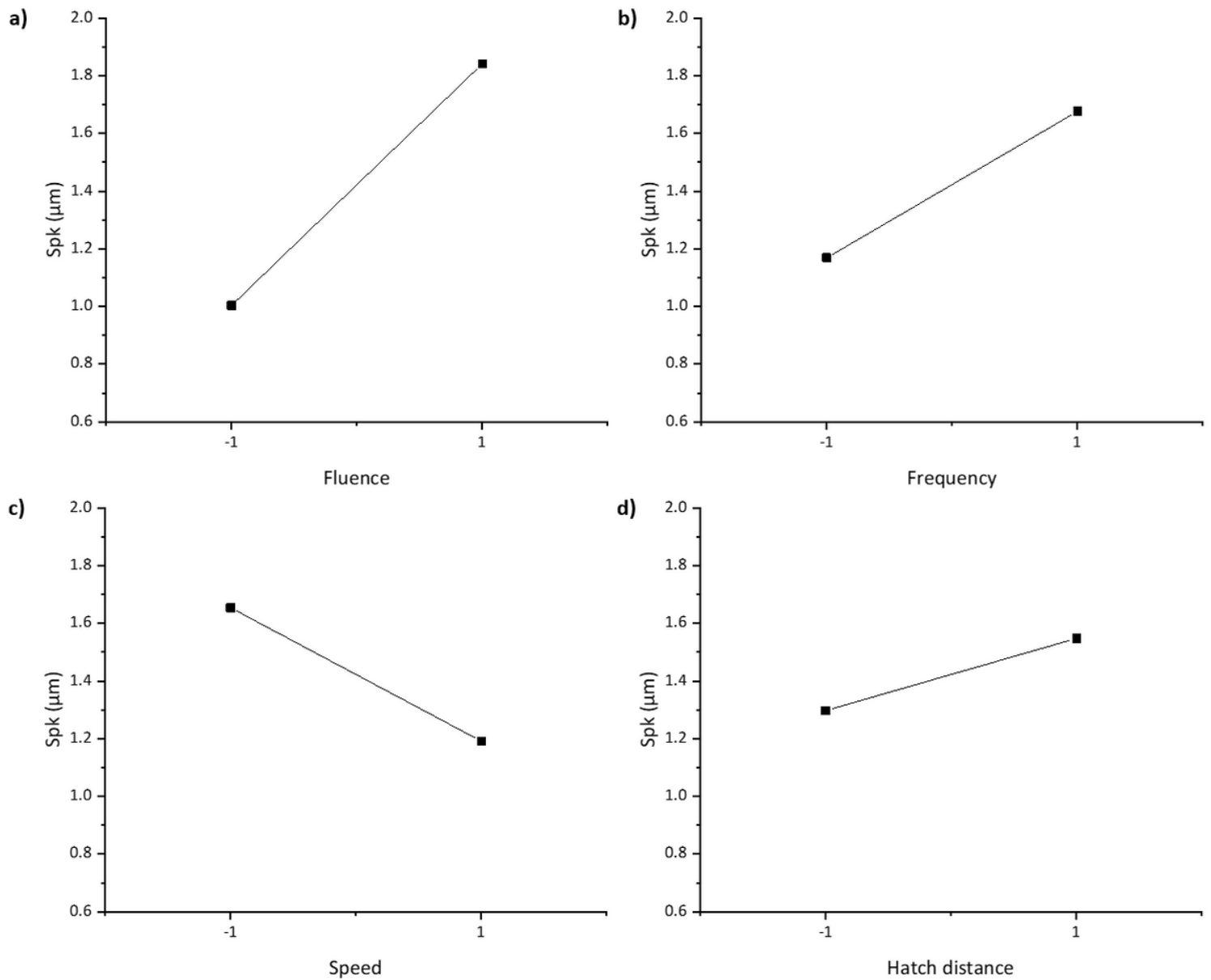


Figure 7

Main effects of each parameters at the two levels set a) Fluence, b) Frequency, c) Speed and d) Hatch distance.

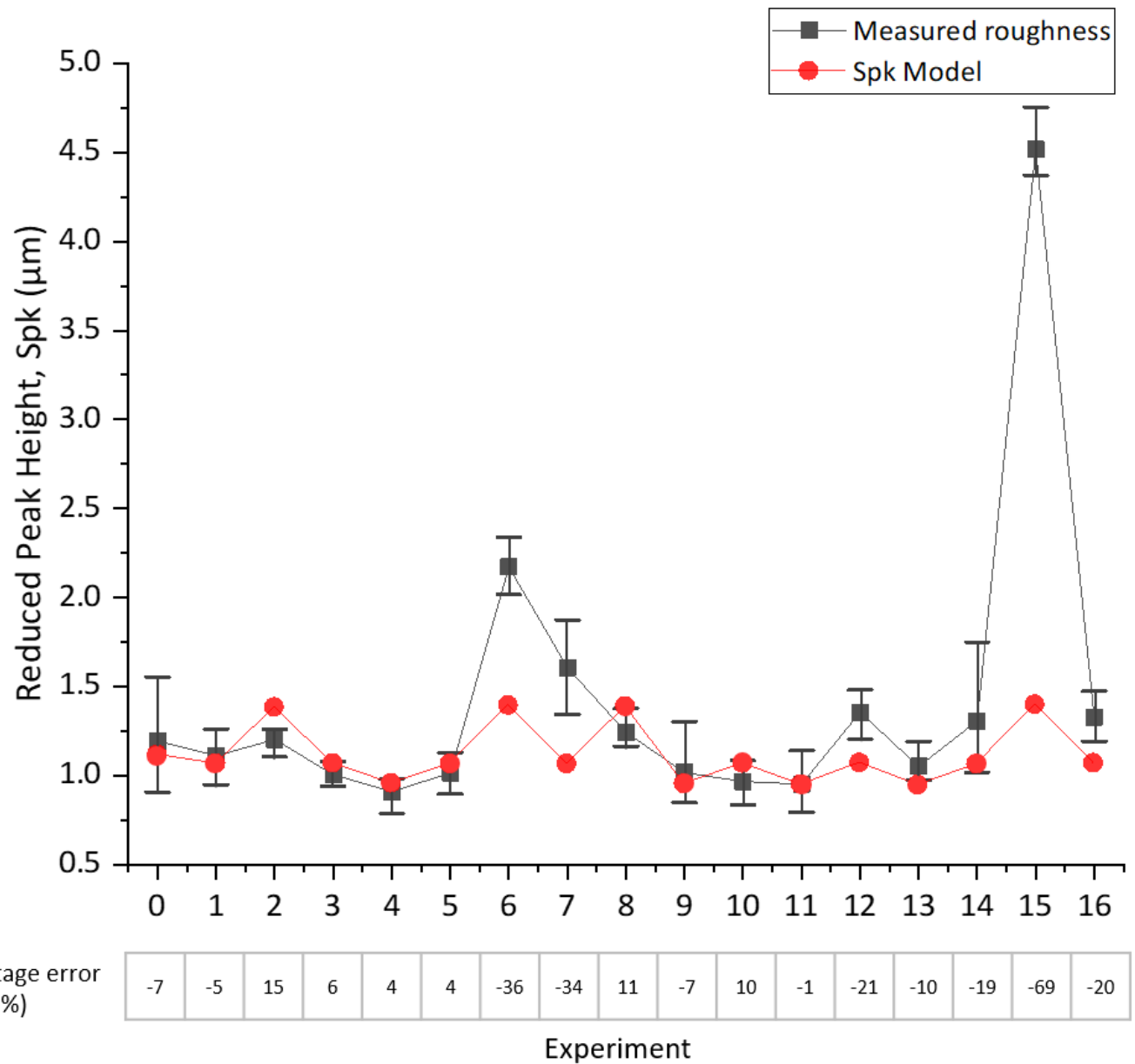


Figure 8

Model compared against Spk results (with error bars) and percentage error.

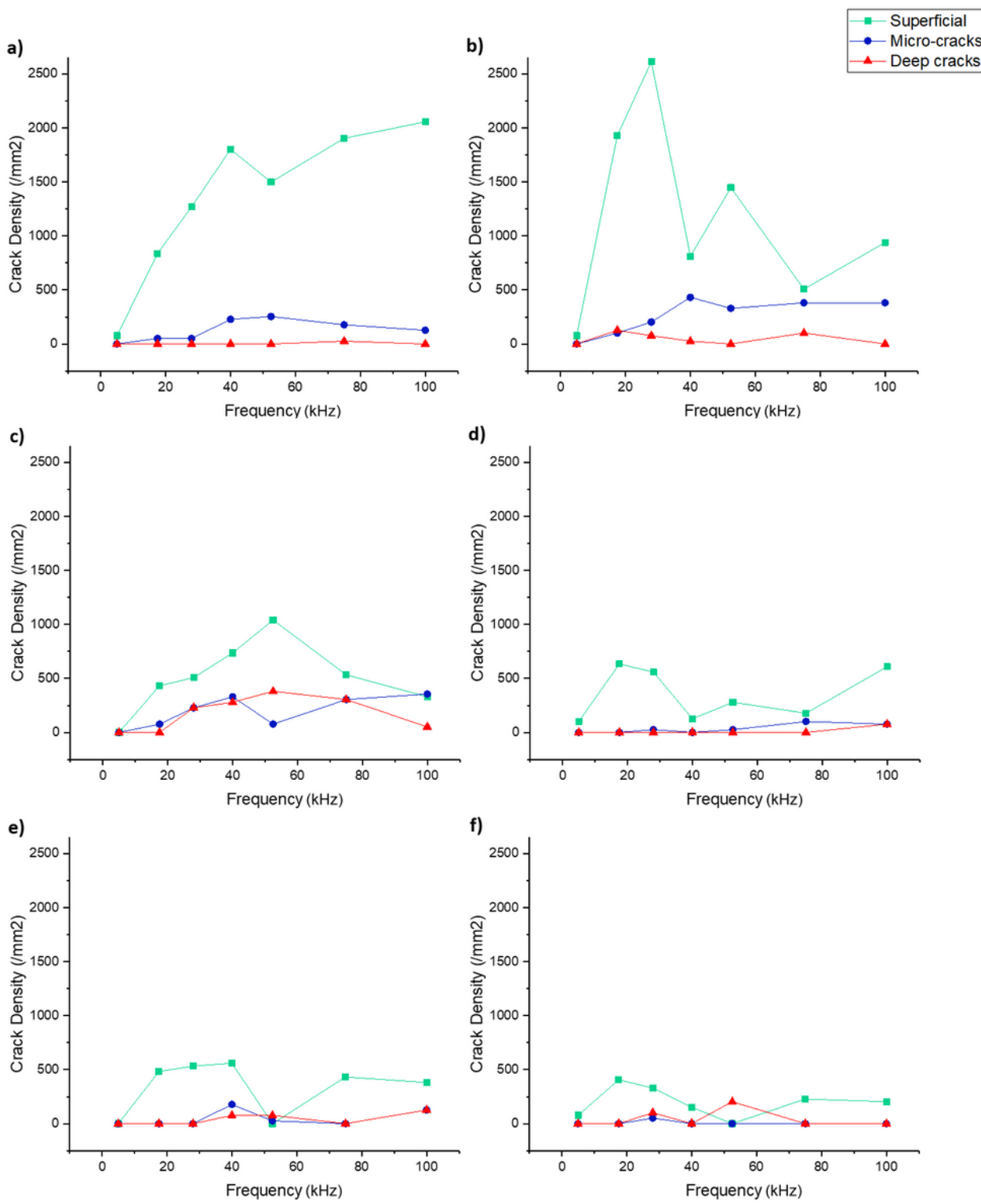


Figure 9

Crack density against frequency at the following fluence settings: a) 0.050 J/cm^2 , b) 0.070 J/cm^2 , c) 0.099 J/cm^2 , d) 0.135 J/cm^2 , e) 0.149 J/cm^2 , f) 0.200 J/cm^2 (Speed 500 mm/s, Hatch distance 0.02 mm).

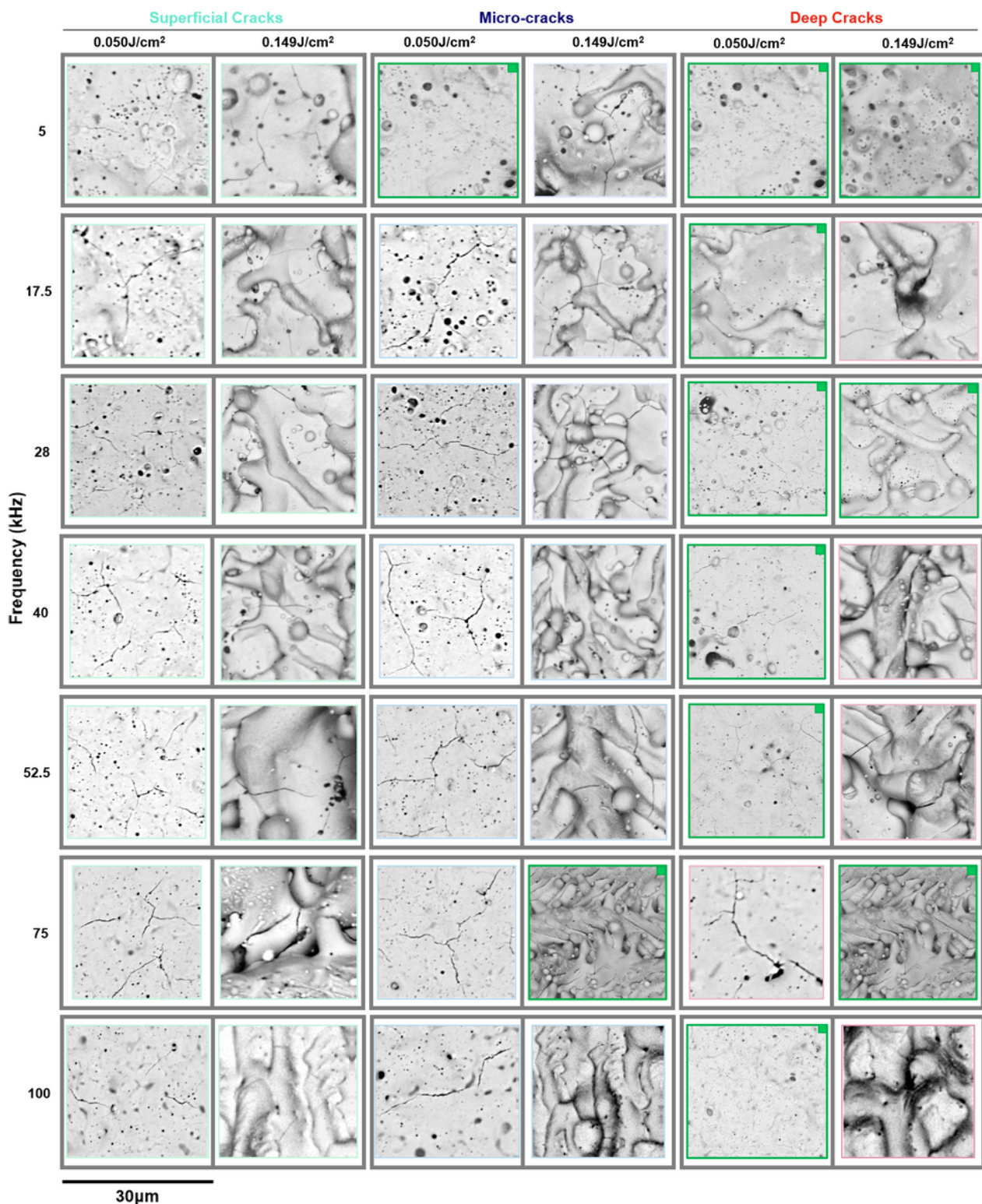


Figure 10

Crack classification against different fluence and frequency settings, diagrams with a green square mark did not present cracks of that type.

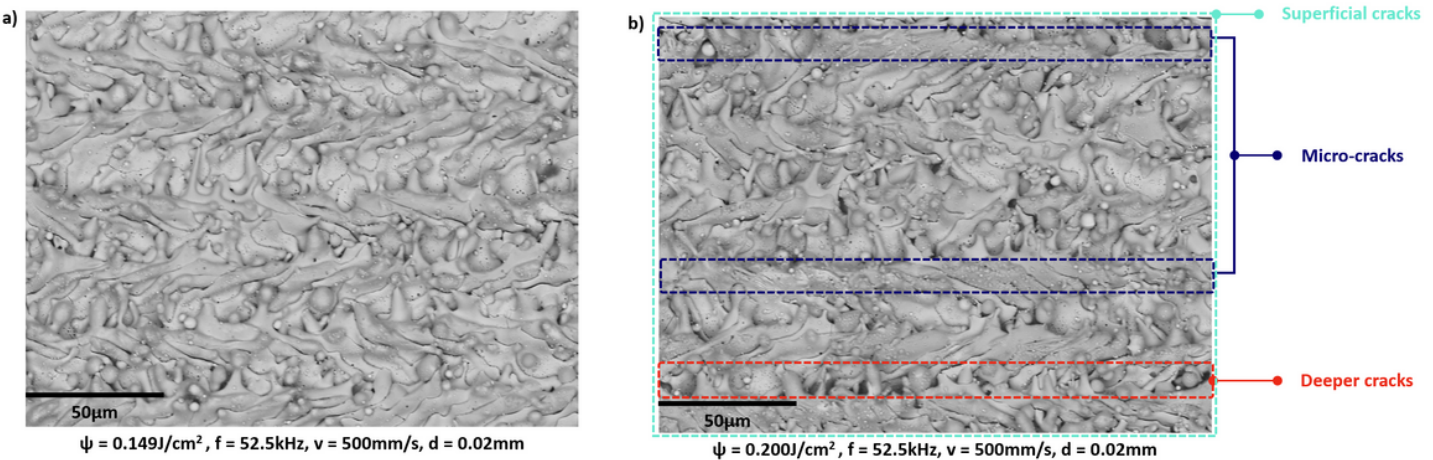


Figure 11

a) Minimal cracks with uniform processing, b) Typical location of each type of crack identified.

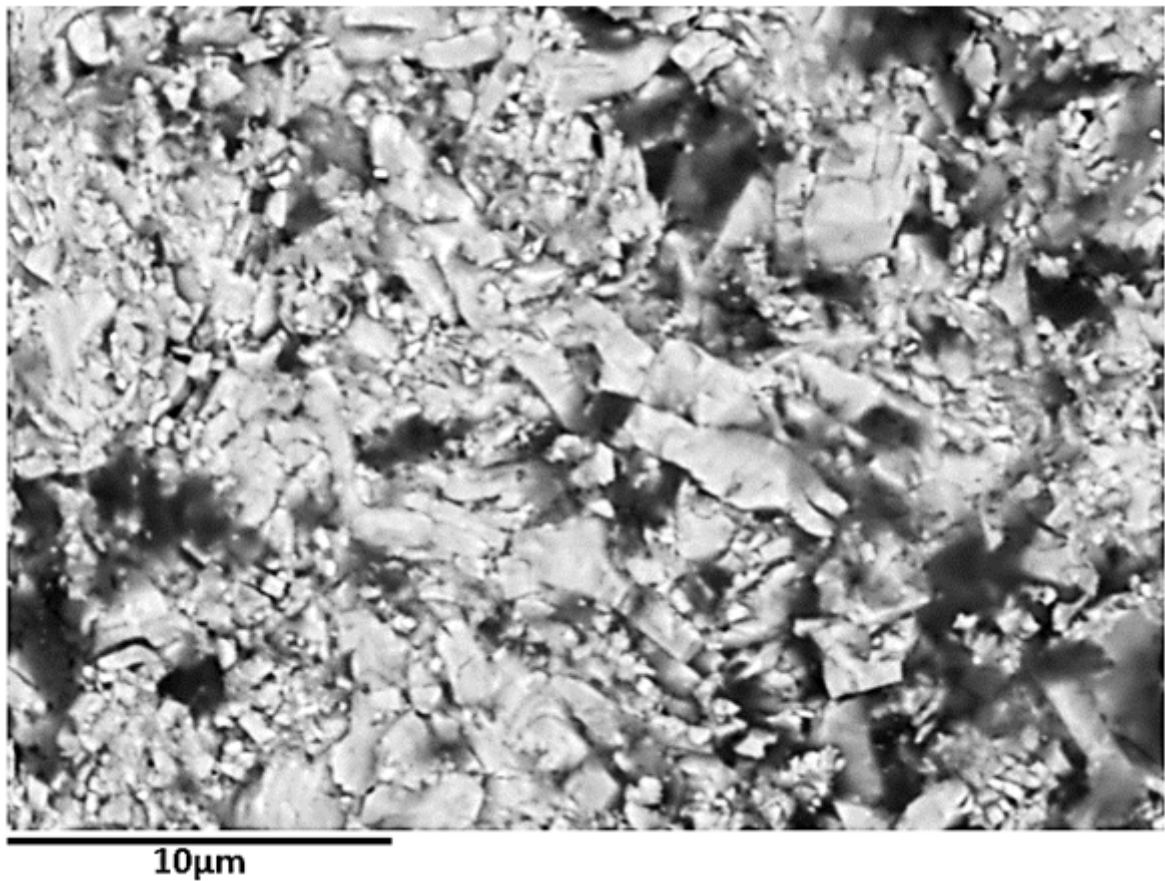


Figure 12

Microstructure of the as-received WC sample.

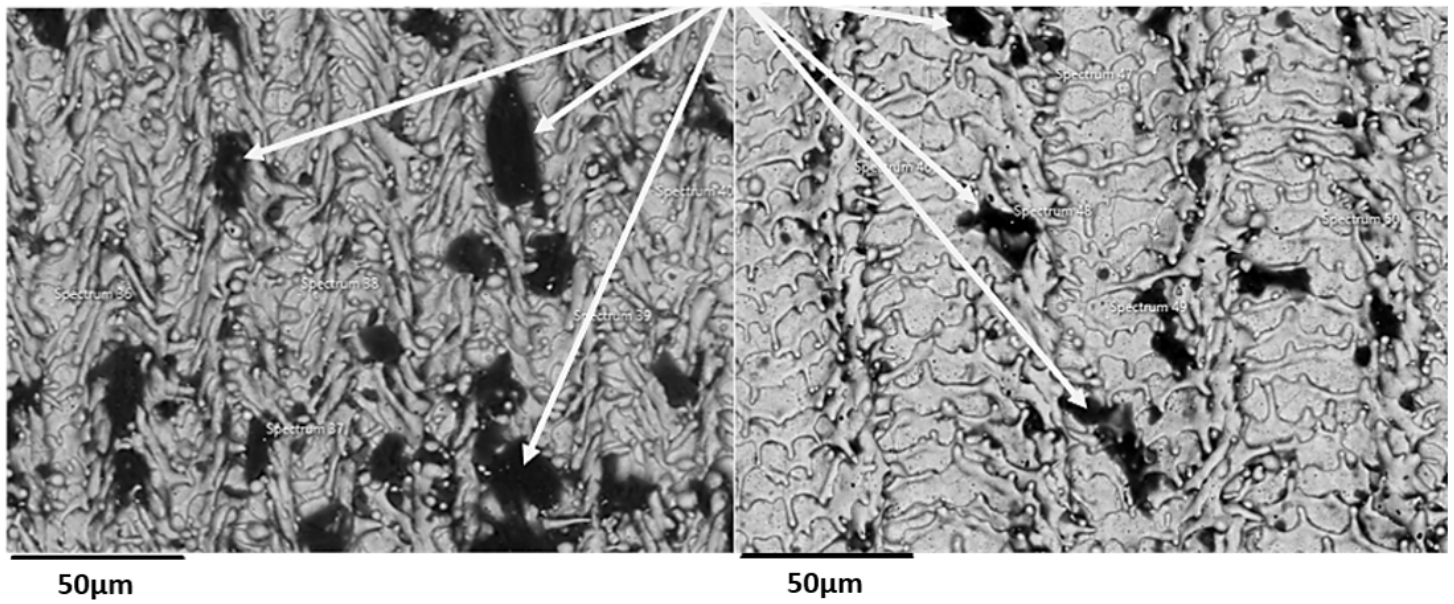


Figure 13

Burnt regions in samples.

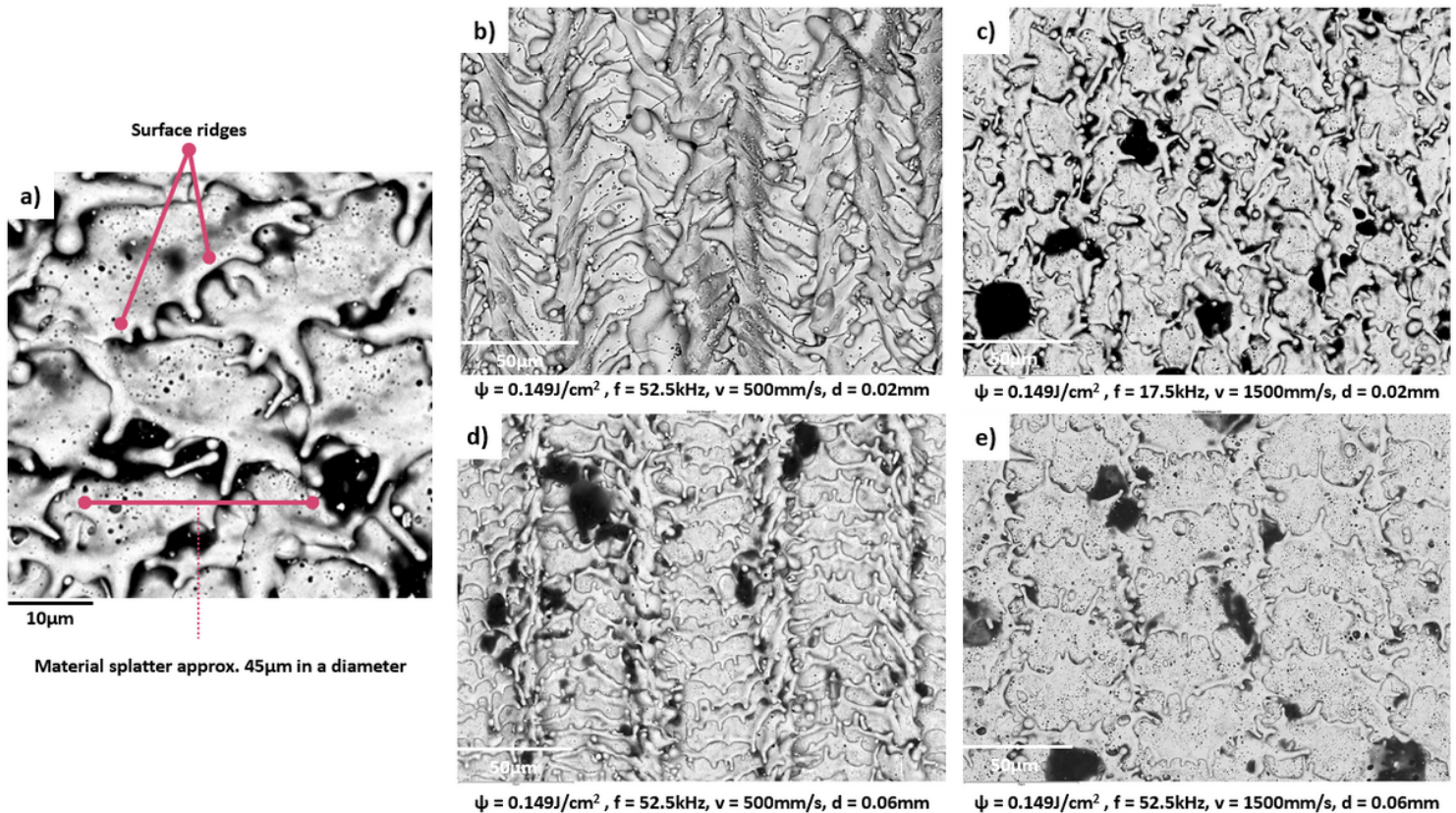


Figure 14

a) Surface remelting and splatter geometry from laser processing, b) Experiment 6, c) Experiment 7, d) Experiment 15, e) Experiment 16.

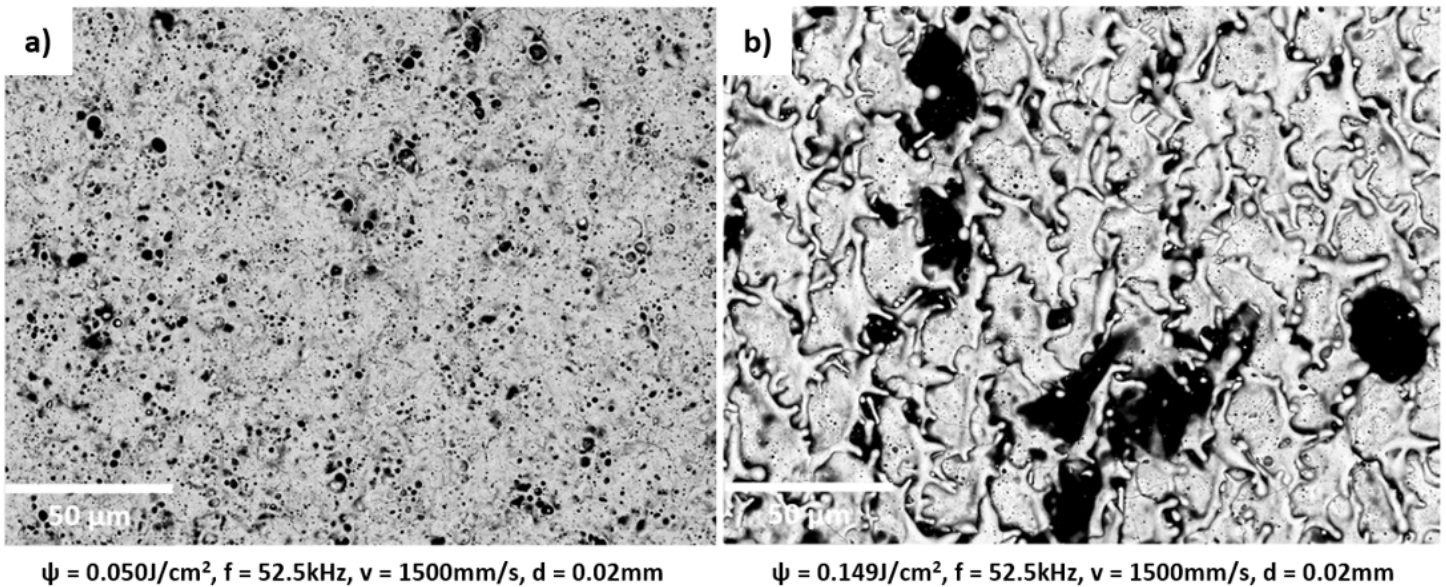


Figure 15

a) Experiment 9 and b) Experiment 12.

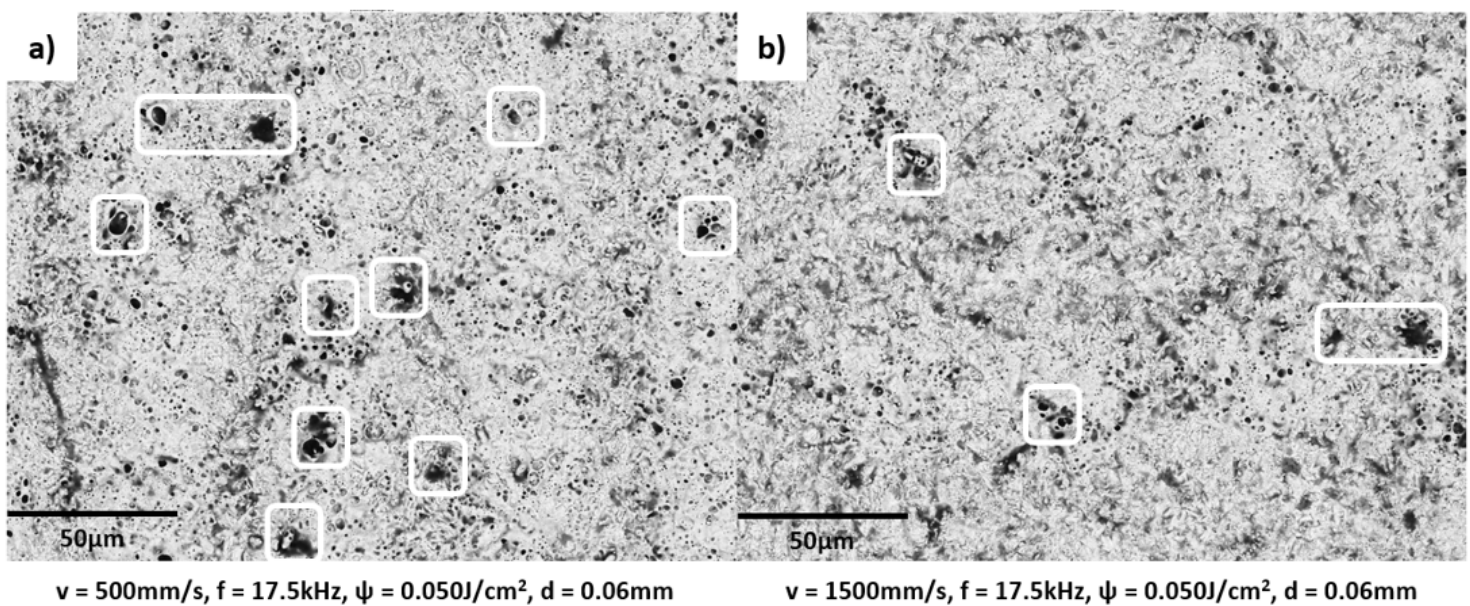


Figure 16

a) Experiment 5, b) Experiment 11. White squares represent localised defects.

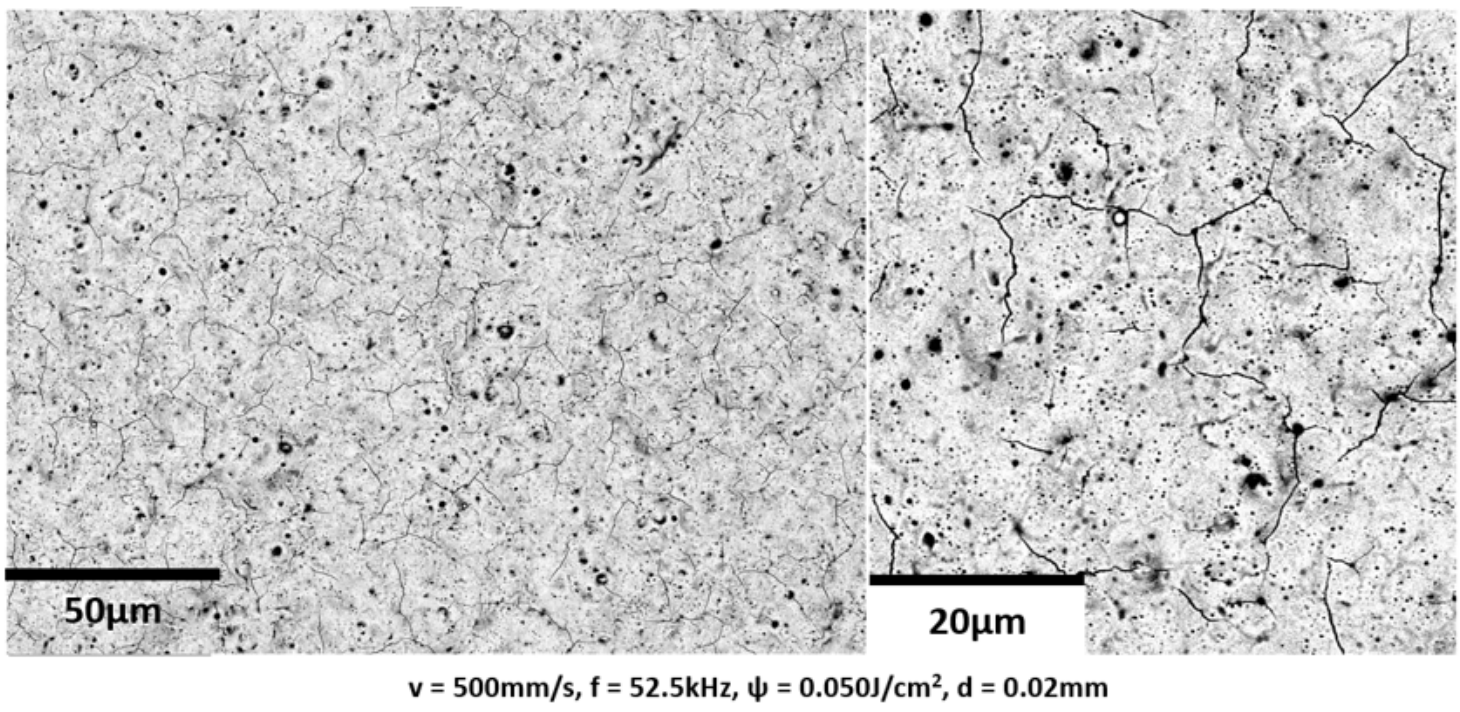


Figure 17

Thermal shock demonstrated in Experiment 3.

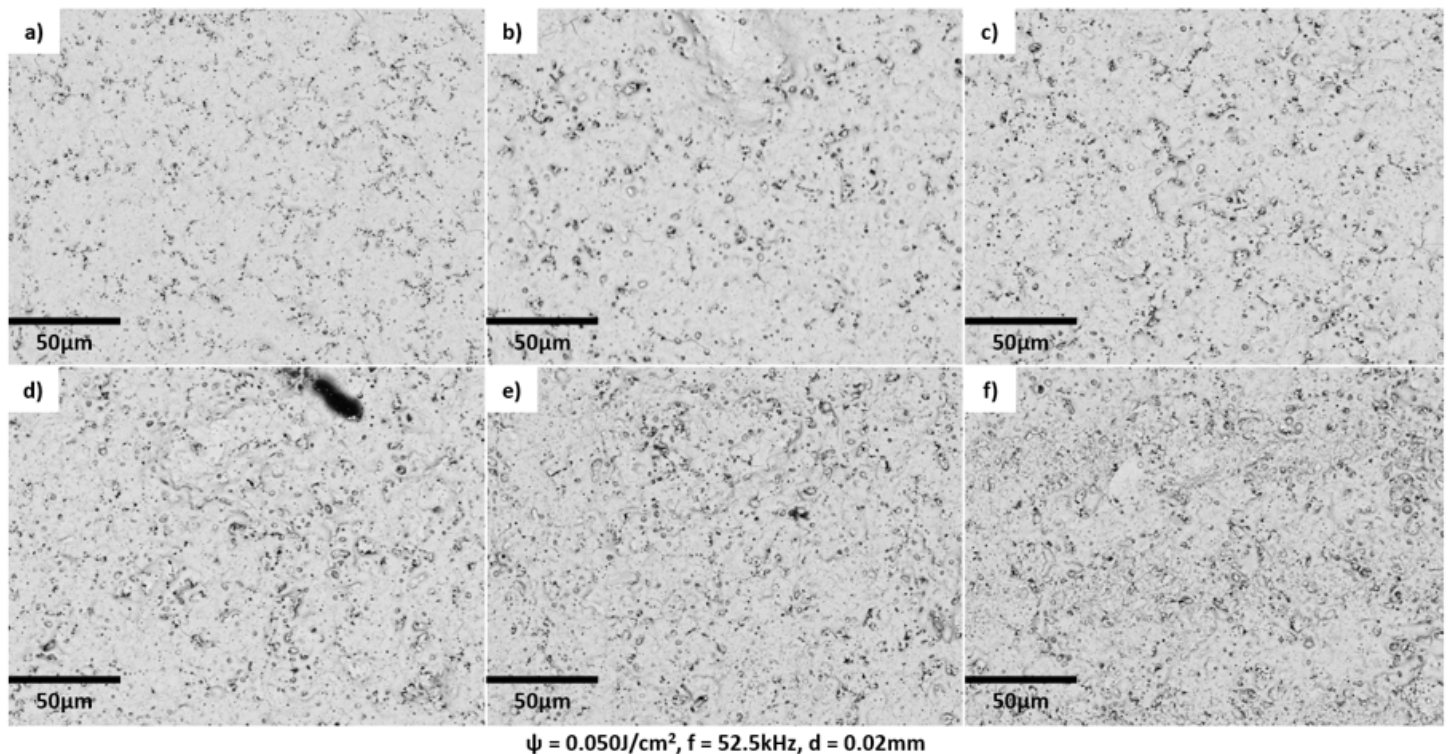
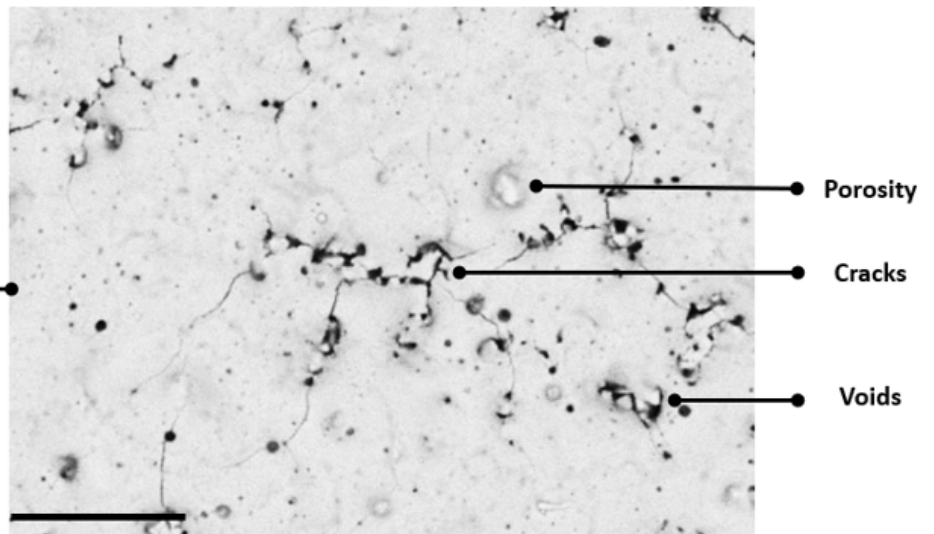
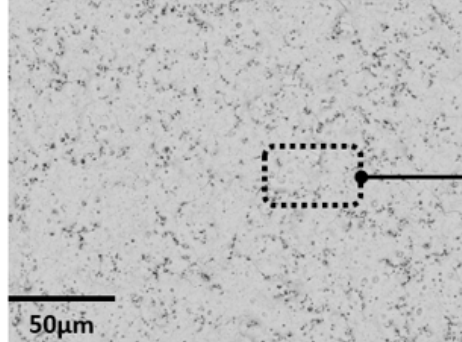


Figure 18

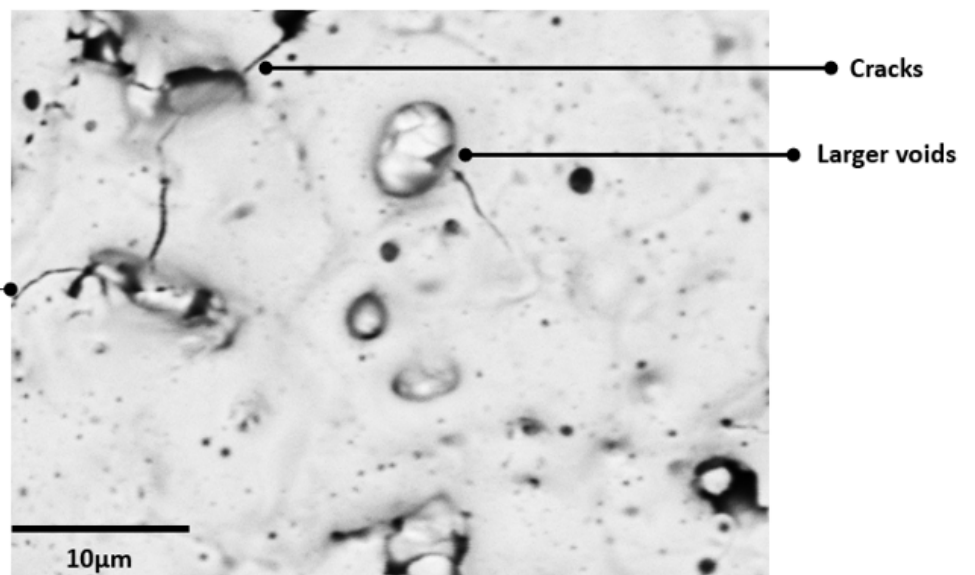
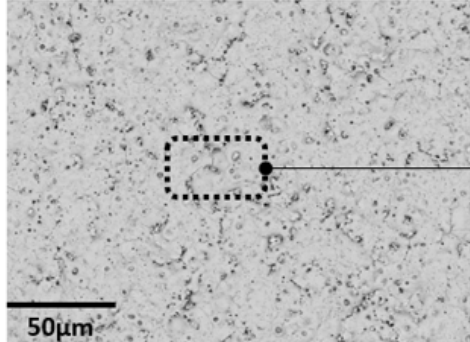
Microstructure of workpiece when processed at different speeds: a) 250 mm/s, b) 500 mm/s, c) 750 mm/s, d) 1000 mm/s, e) 1500 mm/s, f) 2500 mm/s.



$v = 250\text{mm/s}$, $\psi = 0.050\text{J/cm}^2$, $f = 52.5\text{kHz}$, $d = 0.02\text{mm}$

Figure 19

250 mm/s feed speed result.



$v = 750\text{mm/s}$, $\psi = 0.050\text{J/cm}^2$, $f = 52.5\text{kHz}$, $d = 0.02\text{mm}$

Figure 20

750 mm/s feed speed result.

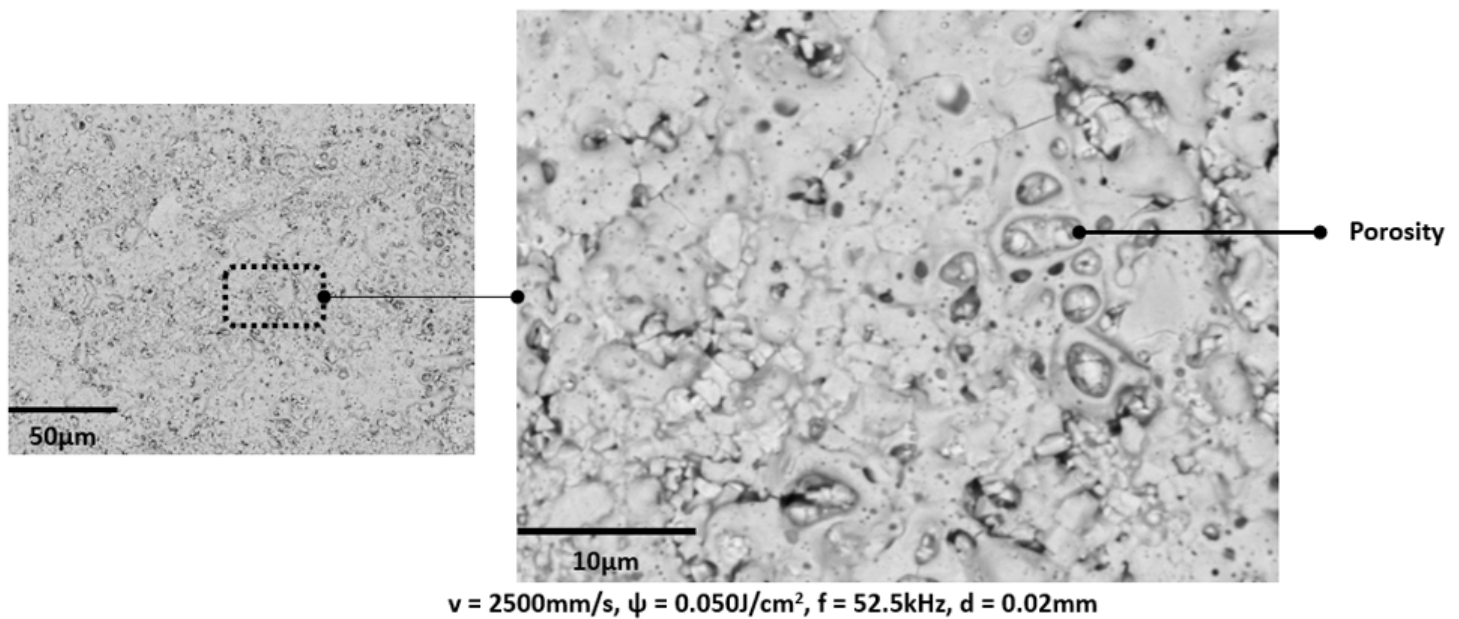


Figure 21

2500 mm/s feed speed result.

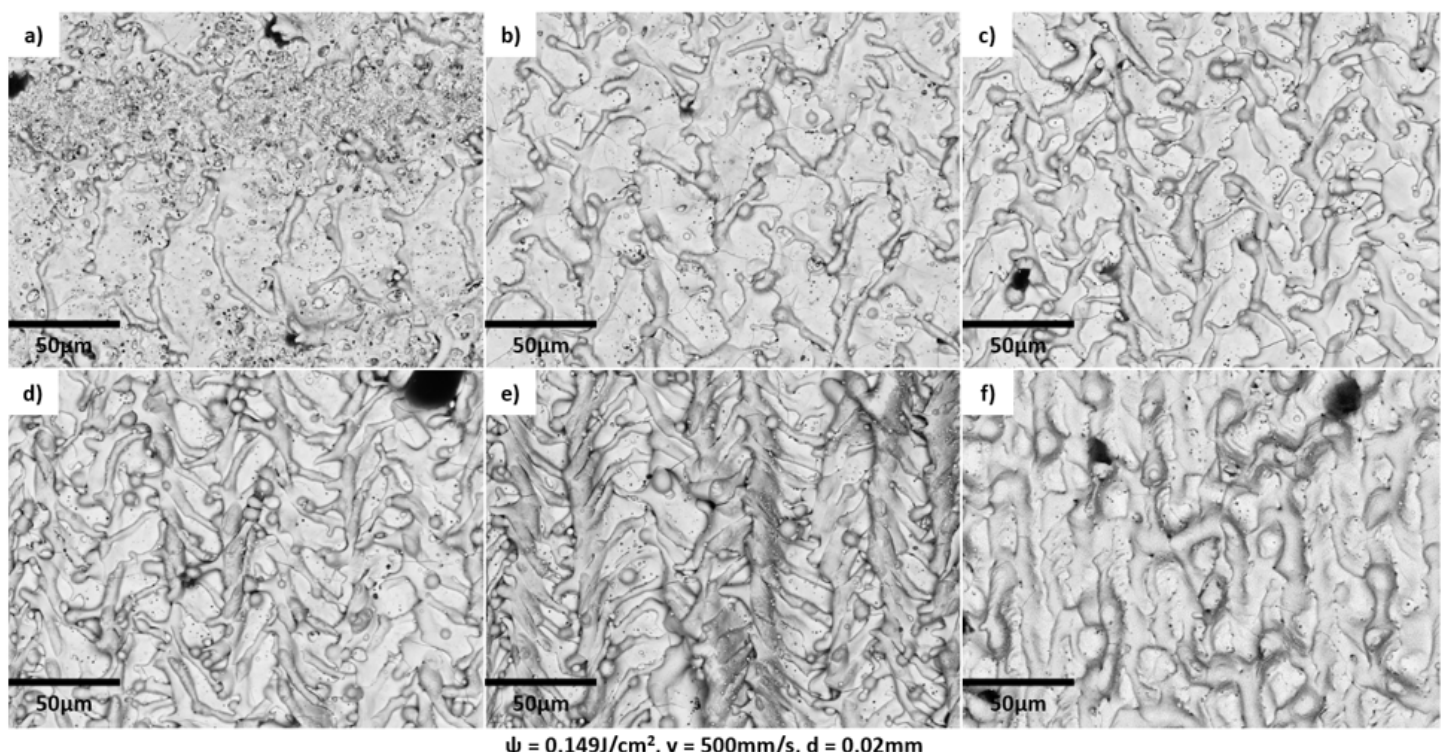


Figure 22

Microstructure of workpiece when processed at different frequencies: a) 5 kHz, b) 17.5 kHz, c) 28 kHz, d) 40 kHz, e) 52.5 kHz and f) 100 kHz.

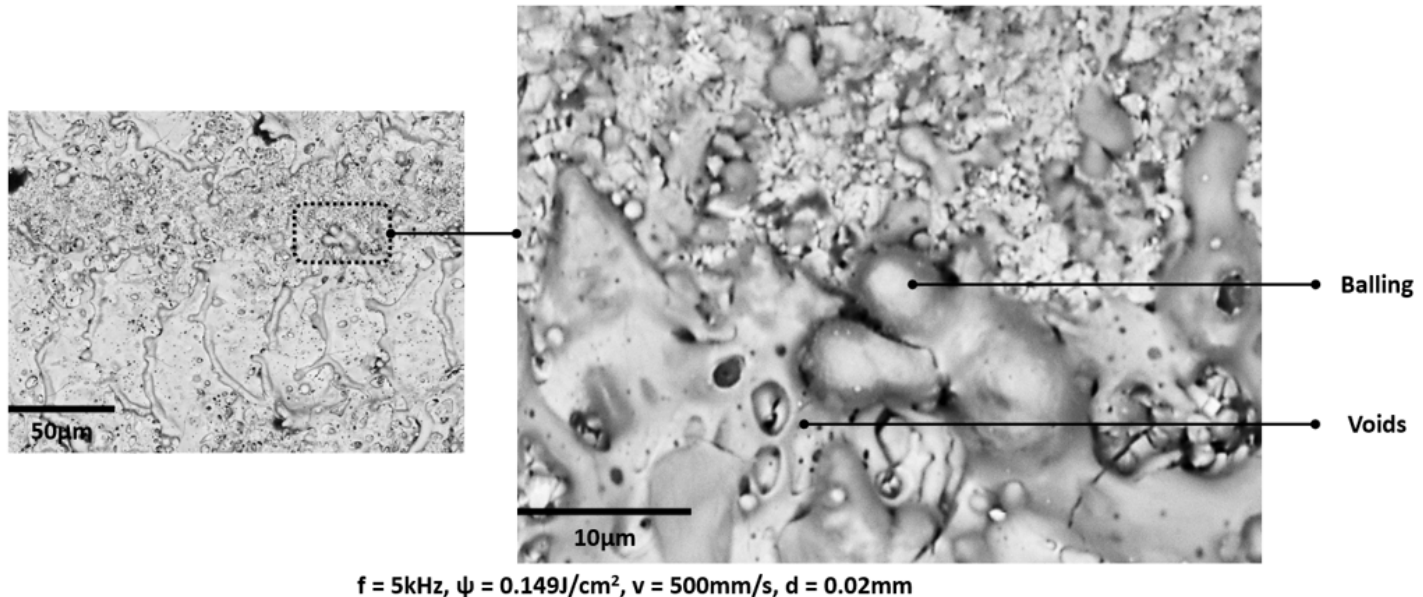


Figure 23

5 kHz frequency result.

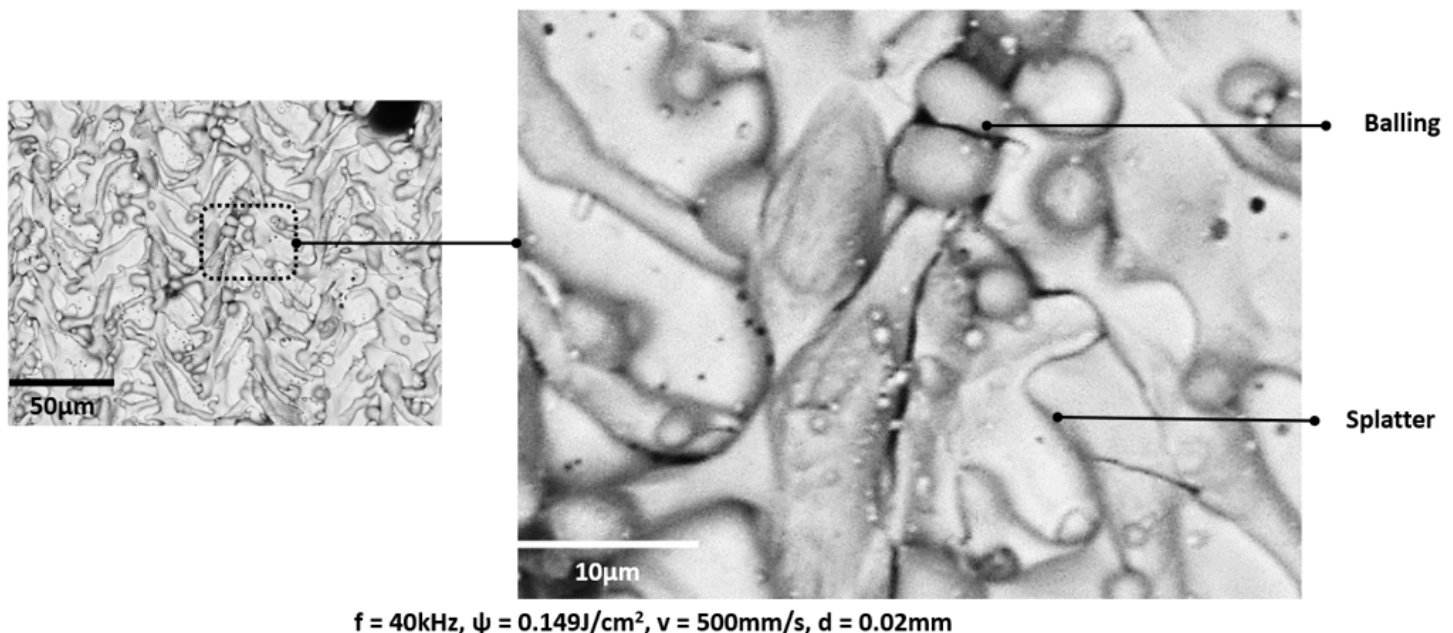


Figure 24

40 kHz frequency result.

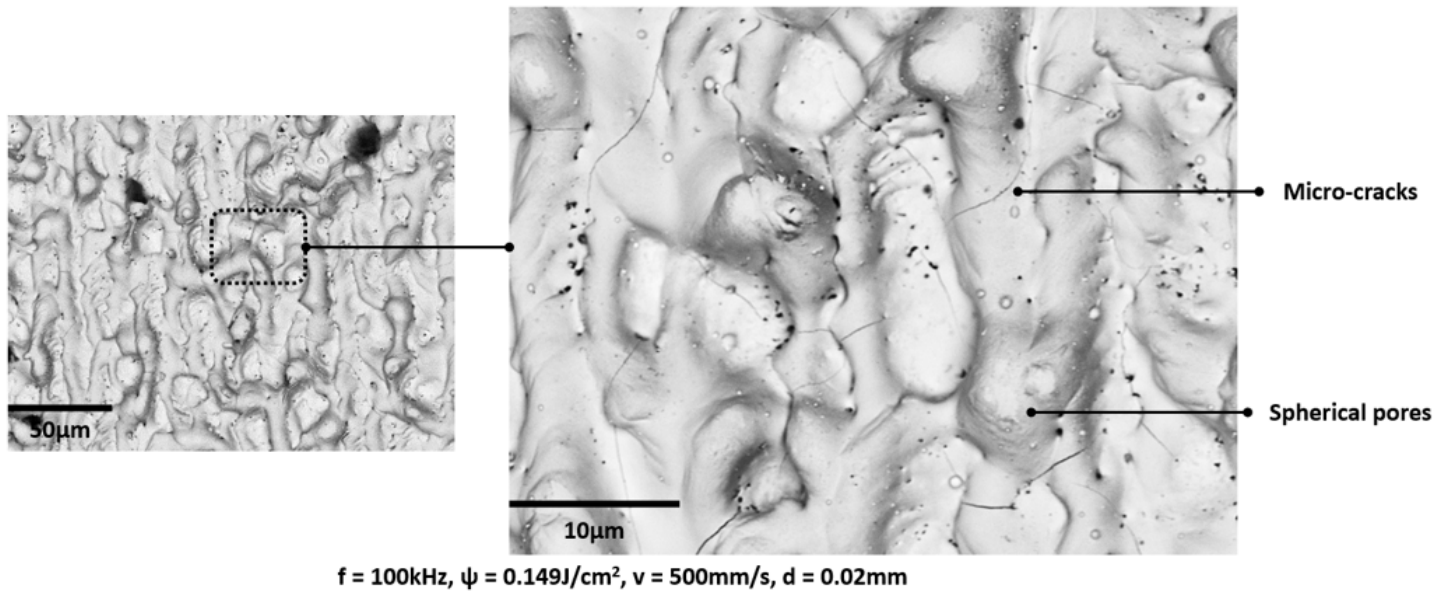


Figure 25

100 kHz frequency result.

Supplementary Files

This is a list of supplementary files associated with this preprint. Click to download.

- [supplementarydatafile.xlsx](#)